remote sensing

MDPI

Article

Slip-Surface Depth Inversion and Influencing Factor Analysis Based on the Integration of InSAR and GeoDetector: A Case Study of Typical Creep Landslide Groups in Li County

Yue Shen [1], Xianmin Wang [1,2,*], Xiaoyu Yi [3,4], Li Cao [5,6] and Haixiang Guo [7]

1 School of Geophysics and Geomatics, China University of Geosciences, Wuhan 430074, China
2 Key Laboratory of Geological Survey and Evaluation of Ministry of Education, China University of Geosciences, Wuhan 430074, China
3 State Key Laboratory of Geohazard Prevention and Geoenviroment Protection, Chengdu University of Technology, Chengdu 610059, China
4 College of Earth and Planetary Sciences, Chengdu University of Technology, Chengdu 610059, China
5 Institute of Advanced Studies, China University of Geosciences, Wuhan 430078, China
6 Hunan Second Surveying and Mapping Institute, Changsha 410000, China
7 Laboratory of Natural Disaster Risk Prevention and Emergency Management, School of Economics and Management, China University of Geosciences, Wuhan 430074, China
* Correspondence: wangxianmin@cug.edu.cn

Highlights

What are the main findings?

- The reconstructed 3D slip-surface geometries (32–98 m) reveal systematic depth–topography relationships that distinguish three fundamental mechanical regimes of creeping landslides.
- Elevation exerts primary control on slip-surface depth, while nonlinear amplification among topographic factors governs its spatial heterogeneity.

What are the implications of the main findings?

- Enables the "form-to-state" transition, allowing internal mechanical conditions to be inferred from surface deformation.
- The identified correspondence between slip-surface depth patterns and deformation regimes offers a transferable conceptual framework for interpreting the internal geometry and mechanical organization of creeping landslides in high-relief terrains.

Abstract

Creeping landslides constitute the predominant form of long-term, slow-moving geohazards in high mountain gorge regions. Under the combined influence of gravity and external triggering factors, these landslides undergo persistent deformation, posing continuous threats to major transportation corridors, hydropower infrastructures, and nearby settlements. Li County is located within the active tectonic belt along the eastern margin of the Tibetan Plateau, characterized by highly variable topography, intensely fractured rock masses, and dense development of creeping landslides. The slip surfaces are typically deeply buried and concealed. Consequently, conventional drilling and profile-based investigations, limited by high costs, sparse sampling points, and poor spatial continuity, are insufficient for identifying the deep-seated structures of such landslides. To address this challenge, this study applies Small Baseline Subset Interferometric Synthetic Aperture Radar (SBAS-InSAR) to obtain ascending and descending deformation rate fields for 2022–2024, revealing pronounced spatial heterogeneity and persistent activity across three types of landslides. Based on the principle of mass conservation, the sliding-surface depths

Check for updates

Academic Editor: Alex Hay-Man Ng

Received: 8 December 2025
Revised: 17 January 2026
Accepted: 19 January 2026
Published: 22 January 2026

Copyright: © 2026 by the authors. Licensee MDPI, Basel, Switzerland. This article is an open access article distributed under the terms and conditions of the Creative Commons Attribution (CC BY) license.

of eight typical landslides were inverted, revealing pronounced heterogeneity. The maximum sliding-surface depths range from 32 to 98 m and show strong agreement with borehole and profile data ($R^2 > 0.92$; RMSE ±4.96–±16.56 m), confirming the reliability of the inversion method. The GeoDetector model was used to quantitatively evaluate the dominant factors controlling landslide depth. Elevation was identified as the primary control factor, while slope aspect exhibited significant influence in several landslides. All factor combinations showed either "bi-factor enhancement" or "nonlinear enhancement", indicating that slip-surface depth is governed by synergistic interactions among multiple factors. Boxplot-based statistical analyses further revealed three typical patterns of slip-surface variation with elevation and slope, based on which the landslides were classified into rotational, push-type translational, and traction-type translational categories. By integrating statistical patterns with mechanical models, the study achieves a transition from "form" to "state", enabling inference of the internal mechanical conditions and evolutionary stages from the observed surface morphology. The results of this study provide an effective technical approach for deep structural detection, identification of controlling factors, and stability evaluation of creeping landslides in high mountain gorge environments.

Keywords: SBAS-InSAR; creep-type landslides; slip-surface depth inversion; GeoDetector; influencing mechanism analysis

1. Introduction

As a typical type of long-term deformation hazard in mountainous regions, creeping landslides are generally composed of loose colluvial and residual deposits with a high proportion of fine-grained soils (clay and silt), exhibiting pronounced plasticity and rheological behavior. Under the combined effects of gravity and external triggering factors, the landslide body undergoes slow and persistent plastic deformation, posing long-term threats to the safety of mountain infrastructure, transportation corridors, and hydropower projects [1–3]. Slip-surface depth, as a key parameter reflecting the internal structure and stability state of a landslide, plays a fundamental role in understanding deformation evolution and determining failure criteria [4–7]. However, due to the deeply buried and highly concealed nature of slip surfaces, traditional techniques, such as drilling, trenching, and surface profiling, are limited by sparse sampling points, high cost, and poor spatial continuity [8,9].

In recent years, advances in Interferometric Synthetic Aperture Radar (InSAR) have enabled large-scale, high-precision landslide deformation monitoring [10–13]. Among various approaches, the Small Baseline Subset (SBAS-InSAR) technique utilizes multi-temporal SAR images to retrieve time-series displacement with millimeter-level accuracy and has been widely applied to early landslide detection and activity zoning [14,15]. Existing studies demonstrate a geometric correspondence between surface deformation patterns and slip-surface depth, indicating that InSAR-derived time-series deformation can provide indirect constraints for estimating landslide depth [16–23]. For example, Hu et al. (2018) [21] derived long-term quasi-3D displacement fields for the seasonally slow-moving Crescent Lake landslide and inverted its actively deforming depth. Handwerger et al. (2021) [22] employed pixel offset tracking with NASA/JPL UAVSAR data to map three-dimensional deformation of 134 slow-moving landslides in northern California, and inferred their active depths, volumes, geometric scaling relationships, and frictional strength using volume conservation, concluding that large landslide complexes primarily grow by lateral expansion rather than thickening.

However, most existing studies still remain focused on extracting slip-surface depth at the scale of individual landslides, with limited attention to the regional-scale spatial distribution of slip-surface depth and its underlying controlling factors and formation mechanisms. Therefore, it is necessary to investigate the spatial variability of slip-surface depth across multiple landslide samples and the differential controlling mechanisms under diverse geomorphic and topographic conditions, in order to better understand the distribution patterns and formation mechanisms of slip-surface depth.

Slip-surface depth is jointly controlled by multiple environmental factors, including topography, lithology, vegetation, rainfall, and in situ stress, and its spatial distribution commonly exhibits pronounced heterogeneity [24]. Among these factors, topographic conditions, particularly slope gradient and slope morphology, play a fundamental role in constraining the geometric position and configuration of potential slip surfaces. However, conventional multivariate regression or overlay-based approaches often fail to effectively capture the complex nonlinear coupling among these controlling factors. In recent years, the GeoDetector model has been widely applied in landslide susceptibility assessment, Earth surface process analysis, and ecological environment studies due to its advantages in quantitatively identifying spatial heterogeneity and evaluating the contributions of environmental factors and their interactions [25–27]. Therefore, introducing the GeoDetector model to analyze the spatial differentiation of slip-surface depth facilitates a quantitative assessment of the controlling effects of individual factors and their interactions on slip-surface depth distribution, thereby enhancing the understanding of its formation mechanisms. In particular, in the eastern margin of the Tibetan Plateau—characterized by highly dissected topography, complex lithology, and intense tectonic activity—the spatial heterogeneity of slip-surface depth and its quantitative relationships with multiple environmental factors remain insufficiently investigated, highlighting the need for targeted and systematic integrated analyses.

Li County, located on the eastern margin of the Tibetan Plateau, is characterized by intense tectonic activity, extreme relief, and highly fractured rock masses. Creep landslides are widely distributed in this region and exhibit features such as deep-seated slip surfaces, strongly plastic shear-zone materials, and long deformation cycles [28–30]. To fill these gaps, this study investigates typical creep-type landslides in Li County and proposes an integrated analytical framework combining SBAS-InSAR and the GeoDetector model. First, multi-temporal Sentinel-1 SAR data are used to retrieve time-series deformation fields via SBAS-InSAR, from which slip-surface depth is inferred based on geometric constraints between slope and cumulative deformation. Second, because the selected typical landslides are geographically close and share the same geological background (stratigraphy, lithology, and structural setting), elevation, slope, aspect, and vegetation cover were chosen to construct the spatial dataset. A GeoDetector model was then applied to quantitatively identify the explanatory power of each factor for the spatial differentiation of sliding-surface depth and to reveal their interaction-enhancement patterns. Finally, by integrating the spatial distribution characteristics of sliding-surface depth with analyses of the driving mechanisms, the internal deformation structures and the controlling factors of typical creeping landslides in Li County were elucidated.

The main innovations of this study are as follows: (1) the development of a coupled SBAS-InSAR and GeoDetector framework for slip-surface depth inversion and mechanism identification, enabling integrated inference from surface deformation to subsurface geometry; (2) For the first time in the complex mountainous terrain on the eastern margin of the Tibetan Plateau, this study systematically identifies the spatial differentiation characteristics of sliding-surface depth and reveals its multi-factor coupling mechanisms. (3) A transferable “deformation-factor-structural mechanism” coupled analytical framework is proposed,

providing a scientific basis for internal structural characterization of creeping landslides and for regional geohazard prevention and mitigation.

2. Study Area and Data

2.1. Study Area

The study area is located in Li County, Sichuan Province, a region with frequent geological disasters. Li County lies in northwestern Sichuan and the southeastern part of the Aba Tibetan and Qiang Autonomous Prefecture. Situated at the intersection between the eastern margin of the Tibetan Plateau and the eastern flank of the Qionglai Mountains, it represents a typical alpine canyon terrain. The specific study area covers the major populated towns of Zagunao, Xuecheng, and Weizhou (Figure 1).

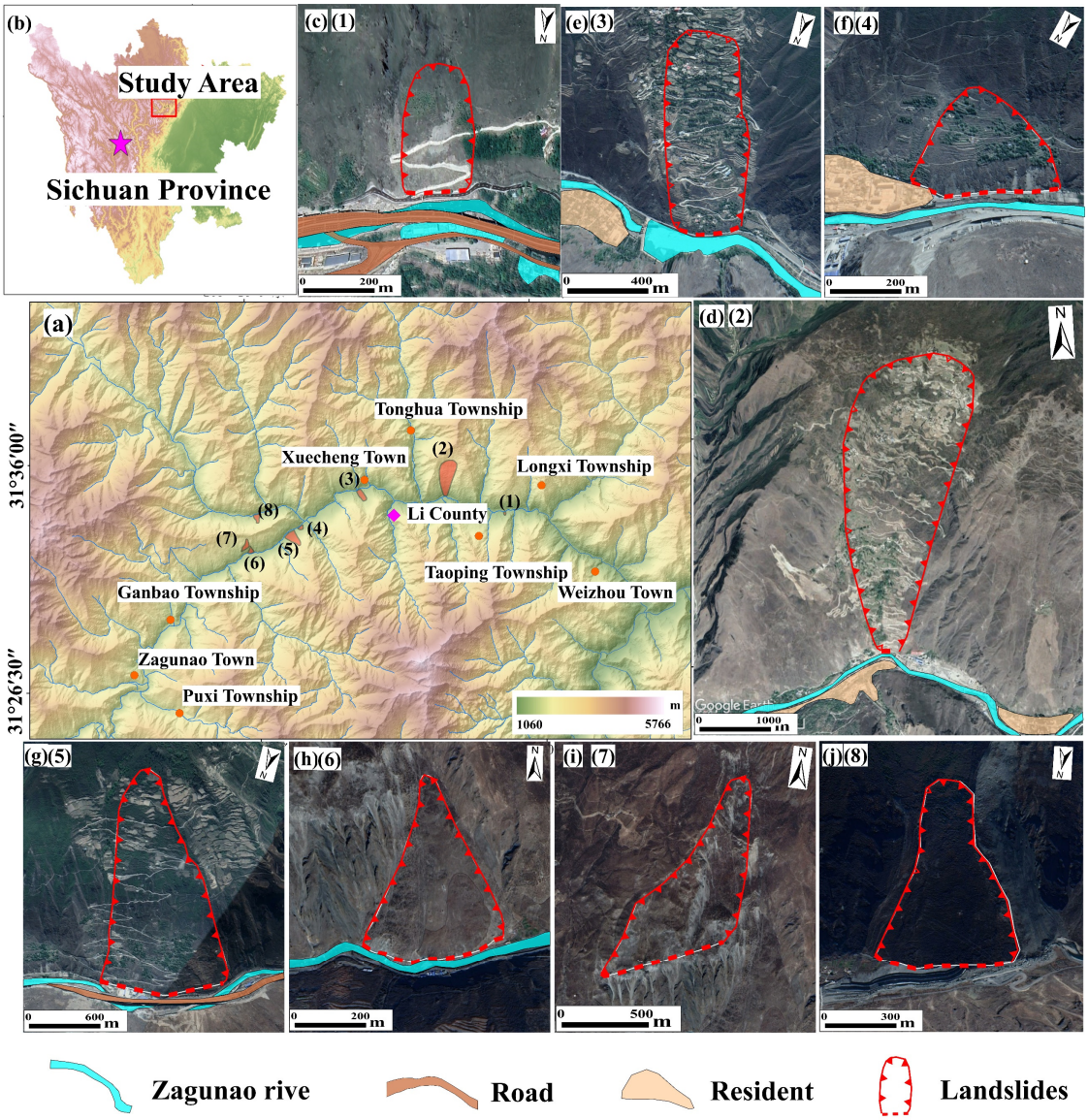


Figure 1. Map of the study area. (**a**) Distribution of typical landslides; (**b**) Geographical location of the study area; (**c**) 3D Google Earth image of the Taopingcun Landslide; (**d**) 3D Google Earth image of the Xishancun Landslide; (**e**) 3D Google Earth image of the Sanzhaicun Landslide; (**f**) 3D Google Earth image of the Mashan Village No. 01 Landslide; (**g**) 3D Google Earth image of the Mashan Village No. 02 Landslide; (**h**) 3D Google Earth image of the Xiaoqi Village No. 01 Landslide; (**i**) 3D Google Earth image of the Xiaoqi Village No. 02 Landslide; (**j**) 3D Google Earth image of the Mengdonggou Landslide.

This region lies in the middle segment of the Longmenshan fault zone and forms an important transition zone between the Tibetan Plateau and the Sichuan Basin. It is characterized by complex geological structures, dense faulting, frequent seismic activity, highly fractured rock masses, and a high susceptibility to geological hazards. Topographically, the terrain generally dips from northwest to southeast with extremely rugged relief and substantial elevation contrasts. The lowest elevation occurs along the Zagunao River valley at approximately 1060 m, while the highest peak reaches 5766 m near the Bipenggou ridge, with an average elevation of about 2700 m (Figure 1). The landscape is dominated by alpine valleys, deeply incised by the northwest-southeast-trending Zagunao River, where the well-developed drainage system provides favorable hydrodynamic conditions for the occurrence of geological hazards. Consequently, the region exhibits a fragile geological environment with diverse and frequent hazards, posing significant threats to local communities and the region's sustainable development.

Eight representative creep-type landslides showing pronounced deformation signals were selected within the study area as typical research objects, with detailed geographic information listed in Table 1. These landslides are primarily distributed along the middle-lower mountain slopes on both sides of the Zagunao River and exhibit a generally elongated, belt-like spatial pattern. High-resolution remote sensing imagery and DEMs show that the landslides possess clear boundaries and well-preserved morphological features (Figure 1b–j). Most of them are situated adjacent to the Zagunao River and the riverbank highway, while residential areas, farmland, and various engineering structures are distributed both upslope and downslope. Intensive human activity leads to strong surface disturbance. Once overall sliding or localized acceleration occurs, the landslides could easily block transportation routes, damage residential buildings and infrastructure, and even induce river blockage or secondary landslide-dam flooding. These processes pose severe risks to residents' lives and property and threaten the safety of regional transportation corridors.

Table 1. Summary of detailed information on the landslides.

No.	Landslide Name	Longitude	Latitude	Area (m^2)
1	Taopingcun Landslide	103°28′22″	31°33′12″	36,390
2	Xishancun Landslide	103°25′33″	31°34′49″	2,496,014
3	Sanzhaicun Landslide	103°21′14″	31°34′13″	362,735
4	Ma Mountain No. 1 Landslide	103°18′22″	31°32′58″	92,574
5	Ma Mountain No. 2 Landslide	103°17′59″	31°32′29″	715,087
6	Xiaoxi No. 1 Landslide	103°15′50″	31°32′06″	140,492
7	Xiaoxi No. 2 Landslide	103°15′35″	31°32′18″	226,310
8	Mengdonggou Landslide	103°16′13″	31°33′26″	231,498

2.2. Data

This study employed Sentinel-1 SAR data from the Copernicus program of the European Space Agency to perform SBAS-InSAR processing and retrieve surface deformation from January 2022 to October 2024. A total of 96 SLC images were acquired, including 44 ascending and 52 descending scenes, all in C-band, VV polarization, and Interferometric Wide Swath (IW) mode, with a single-look spatial resolution of approximately 5 m × 20 m and a swath width of 250 km. The 30 m SRTM DEM was used for topographic correction and removal of terrain effects. Google Earth optical imagery and high-resolution topographic data were utilized to assist in interpreting landslide geomorphological features. In addition, ALOS DEM and multi-year mean vegetation coverage data were incorporated for velocity decomposition, slope-aspect calculation, and analysis of the influencing factors (Table 2). Software Version: MATLAB2019b, ArcGIS10.5, ENVI5.6.

Table 2. Multisource data employed in this work.

Data	Time	Quantity	Resolution Data Source	Data Source	Purpose
Sentinel-1A SAR image	Ascend: January 2022–October 2024 Descent: January 2022–October 2024	44 52	5 × 20 m	Alaska Satellite Facility (ASF), Fairbanks, AK, USA	InSAR data processing
SRTM DEM	2000	1	30 m	U.S. Geological Survey (USGS), Reston, VA, USA	InSAR data processing
Google Earth image	September 2019	1	1 m	Google Earth, Mountain View, CA, USA	Obtain the terrain and topography of landslide hazards
ALOS_DEM	2011	1	12.5 m	Japan Aerospace Exploration Agency (JAXA), Chofu, Tokyo, Japan	Slope and aspect calculation and driving factor analysis
Vegetation coverage	2022	1	30 m	National Tibetan Plateau Data Center (TPDC), Institute of Tibetan Plateau Research, Chinese Academy of Sciences, Beijing, China	Influencing factor analysis

3. Methodology

Based on the above research background, this study focuses on typical creep-type landslides in Li County on the eastern margin of the Tibetan Plateau and develops an integrated multi-source data analysis framework that combines SBAS-InSAR techniques with the GeoDetector model (Figure 2). First, multi-temporal Sentinel-1 SAR images are processed using SBAS-InSAR to obtain high spatiotemporal resolution time-series deformation fields of the landslides. The spatial distribution of slip-surface depth is then inferred by incorporating geometric constraints between local slope and cumulative displacement. Second, a spatial dataset is constructed using terrain and environmental factors including elevation, slope, aspect, and vegetation cover. The GeoDetector model is applied to quantitatively determine the explanatory power of each factor on the spatial variability of slip-surface depth and to reveal their interaction patterns. Finally, by integrating the inverted slip-surface depth with the identified controlling factors, the internal deformation structure and formation mechanisms of the typical creep landslides in the study area are systematically analyzed, thereby elucidating their deformation evolution under multi-factor coupling.

This study provides a novel methodological pathway and theoretical reference for detecting slip-surface characteristics and quantitatively deciphering the driving mechanisms of creep-type landslides in complex mountainous regions, offering significant implications for refined geohazard monitoring and risk assessment.

3.1. Slip-Surface Depth Inversion Method

Based on ascending and descending Sentinel-1A SAR images acquired from January 2022 to October 2024, this study retrieved the annual mean deformation rate of the landslides using the SBAS-InSAR technique. Interferometric pairs were generated using a temporal baseline of 36 days, and the shortest 3% of spatial baselines were selected to form the interferometric network, thereby constructing a high-reliability short-baseline time-series analysis dataset. During data processing, filtering, phase unwrapping, and removal of residual phase ramps using stable control points were performed to accurately extract the LOS deformation rates across the study area.

A two-dimensional deformation decomposition model was then introduced. By integrating the average slope and aspect extracted from the ALOS DEM with the imaging geometries of the ascending and descending tracks (including incidence angle and azimuth

angle), the LOS deformation was successfully decomposed into two key components: the downslope (slope-parallel) and slope-normal directions (Equation (1)). This decomposition effectively eliminates the influence of terrain and satellite viewing geometry, resulting in a 2D deformation field that more realistically reflects the gravity-driven movement characteristics of the landslides. The improved deformation field provides precise spatiotemporal constraints for hazard identification and mechanism analysis.

$$D_{\mathrm{LOS}} = \begin{bmatrix} a & c \end{bmatrix} \begin{bmatrix} D_{slp} \\ D_{nor} \end{bmatrix}$$

$$\begin{aligned} a = \cos\theta\ \cos\alpha\ \sin\beta + \sin\theta\ \sin\varphi\ \cos\alpha\ \cos\beta + \\ \sin\theta\ \cos\varphi\ \sin\alpha \end{aligned} \tag{1}$$

$$\begin{aligned} c = \cos\theta\ \sin\alpha\ \sin\beta + \sin\theta\ \sin\varphi\ \sin\alpha\ \cos\beta - \\ \sin\theta\ \cos\varphi\ \cos\alpha \end{aligned}$$

where a and c are the projection coefficients of deformation in the slope-parallel and slope-normal components, respectively; D_{slp} and D_{nor} represent the slope-parallel and slope-normal components to be solved, respectively; α and β denote the average slope angle and aspect of the landslide; and θ and φ correspond to the radar incidence angle and satellite flight (azimuth) angle, respectively.

Creeping landslides are typically composed of loose colluvial and residual deposits with a high proportion of fine-grained soils (clay and silt), exhibiting pronounced plasticity and rheological behavior. Therefore, the landslide slip-surface depth is inverted based on the law of mass conservation by integrating the decomposed slope-parallel and slope-normal deformation rates. The core concept is that when a landslide body is regarded as a continuous medium with constant density, incompressibility, and no significant erosion or deposition along its basal surface, the change in mass within the control volume is governed entirely by the divergence of surface material flux, and no mass is lost from the system over time. Accordingly, by performing vertical integration along the landslide surface and basal plane and incorporating appropriate kinematic boundary conditions, the governing Equation (2) can be derived.

$$v_z = -\nabla\cdot(h\overline{v}) \tag{2}$$

In the above equation, the observed surface-normal deformation rate v_z is numerically equal to the negative divergence of the surface velocity vector $\overline{v}$ multiplied by the actively deforming landslide depth h.

For numerical implementation, the governing equation must be discretized. By introducing rheological parameters to relate the internal velocity field to the surface kinematics and applying a central difference scheme, the complex partial differential equation is ultimately transformed into a linear Equation (3) [20–22].

$$\vec{v}_z = \mathrm{A}\cdot\vec{h} \tag{3}$$

The matrix A is constructed using the slope-parallel and slope-normal deformation rate fields (v_x, v_y) together with the sampling interval Δx. During the inversion stage, the depth h is obtained by minimizing the objective Function (4) [20–22].

$$|\,Ah - v_z\,|^2 + \alpha^2\,|\,\nabla^2 h\,|^2. \tag{4}$$

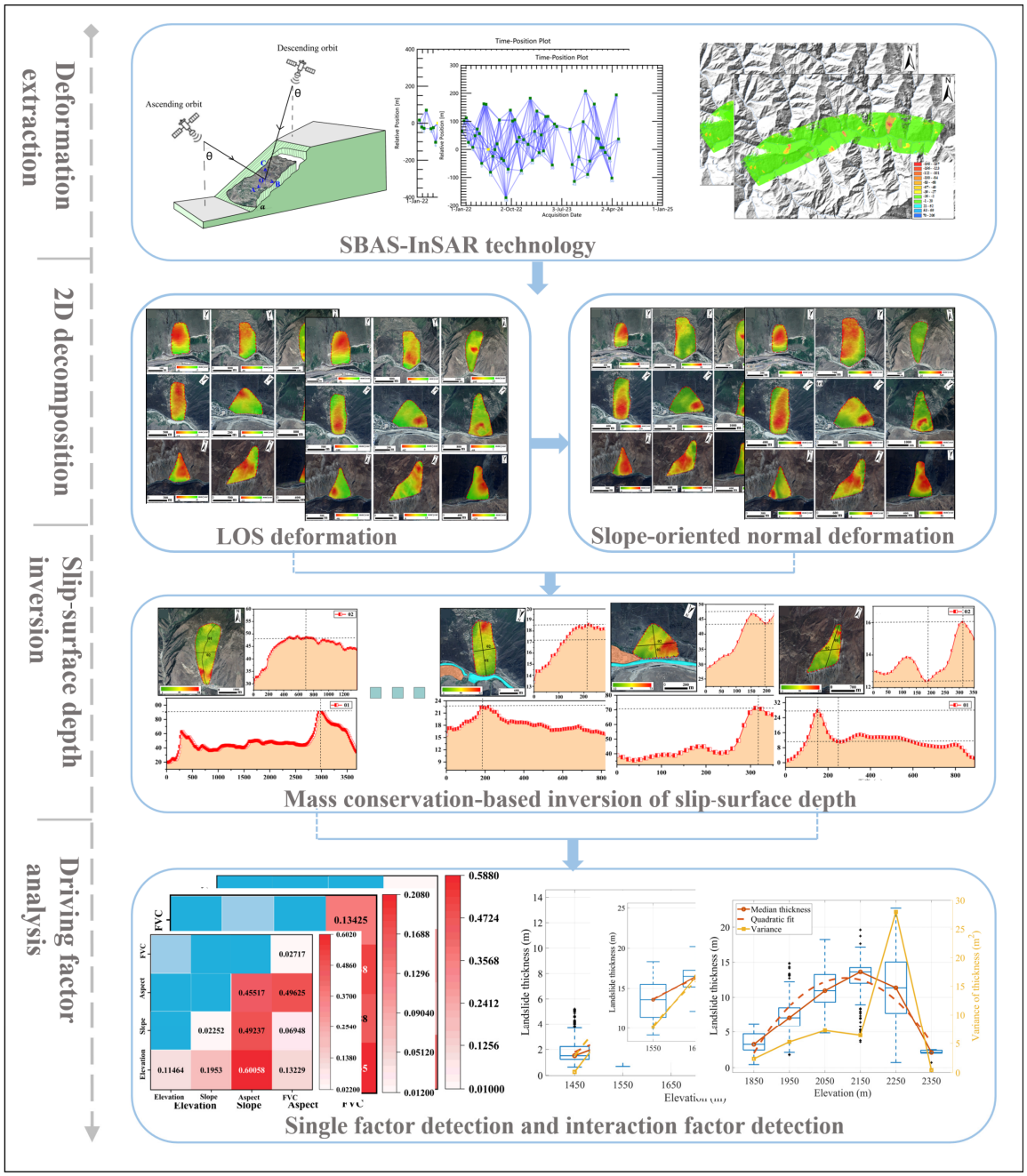


Figure 2. Technical framework.

The objective function essentially corresponds to an L2-norm Tikhonov regularization-based inversion framework. The first term ensures that the inverted thickness is consistent with the observed deformation data, while the second term is a gradient-based regularization constraint on the slip-surface depth, introduced to suppress non-physical oscillations arising from InSAR noise, coherence loss, and data incompleteness. α represents the strength of the smoothness regularization, by which the smoothing factor α is used to suppress solution instability that may be induced by data noise. In terms of parameter selection, α was searched within the range of 10^{-3}–10^{1}, and for each landslide the optimal regularization parameter was determined using the Generalized Cross-Validation (GCV) approach, such that an optimal balance between the data misfit term and the smoothness constraint was achieved, ultimately yielding thickness results that are geologically reasonable and spatially smooth [22].

It should be particularly emphasized that, for creeping landslides, the timescale of deformation evolution commonly spans several decades or even longer. InSAR observations within a limited temporal window are therefore insufficient to fully capture the entire evolutionary process from the onset of creep, through the progressive development of the slip surface, to potential instability. Accordingly, the slip-surface depth inverted in this study should be interpreted as an equivalent slip-surface geometry within the monitoring period or at a recent temporal scale, representing the primary depth range involved in shear deformation during the current deformation stage. Notably, creeping landslides typically exhibit relatively stable annual deformation rates. The approximately three-year InSAR observation period adopted in this study is adequate to characterize the deformation state during the stable creep stage, thereby enabling a relatively reliable inversion of the slip-surface geometry of creeping landslides at the current stage.

3.2. Analysis of Factors Influencing Slip-Surface Depth Method

Wang et al. (2017) proposed the GeoDetector model, a statistical method designed to detect spatial heterogeneity and identify the driving forces behind it [25]. The core concept is that if an independent variable exerts a significant influence on a dependent variable, the two should exhibit similar spatial distribution patterns. Since its introduction, GeoDetector has been widely applied in studies of vegetation cover, drought, landslides, and environmental pollution [31–33]. The GeoDetector framework consists of four components: the factor detector, interaction detector, risk detector, and ecological detector. In this study, the factor detector and interaction detector are employed to analyze the driving factors influencing landslide depth. The factor detector assesses the spatial heterogeneity of the dependent variable and quantifies the explanatory power of each factor with respect to its spatial variation. This explanatory power is expressed by the q-statistic, whose formulation is given in Equation (5).

$$q = 1 - \frac{\sum_{h-1}^{L} N_h \sigma_h^2}{N\sigma^2} = 1 - \frac{SSW}{SST} \quad (5)$$

In the equation, h denotes the number of categories of a variable or factor, where $h = 1, \ldots, L$. Nh and N represent the sample size within category h and the total sample size, respectively. 2σh and 2σ are the variances of the dependent variable within category hhh and across the entire study area. The term $\sum_{h-1}^{L} N_h \sigma_h^2$ represents the within-group sum of squares (SSW), while $N\sigma^2$ represents the total sum of squares (SST). The q-statistic ranges from 0 to 1; a larger q value indicates stronger explanatory power of the factor on the spatial heterogeneity of the dependent variable, whereas a smaller q value indicates weaker explanatory power. When q = 0, the factor has no explanatory effect; when q = 1, the factor fully explains the spatial distribution of the dependent variable [33,34].

The interaction detector is used to evaluate whether two factors jointly enhance or weaken their explanatory power on the dependent variable, or whether the effect of one factor is independent of the other [31]. The q-values of factors X1 and X2, denoted as q1 and q2, are obtained using the factor detector. The interaction detector then computes the interaction q-value of X1 and X2, and compares it with q1 and q2 to determine the type of interaction. Here, Min (q1, q2) denotes the smaller of the two q-values, Max (q1, q2) denotes the larger, and q1 + q2 denotes their sum (Table 3).

In this study, elevation, slope, aspect, and vegetation cover were integrated to analyze their influence on the landslide depth derived in the previous section. The 12.5 m resolution elevation data provided by ALOS-2 were used to calculate slope and aspect. In addition, the annual vegetation coverage data for 2022 were obtained from the National Tibetan Plateau Data Center (https://www.tpdc.ac.cn/allDatadatasetType=all (accessed on 11 April 2024)) (Table 4). The natural breaks (Jenks) classification method was applied

to categorize the discretized data. By minimizing within-class variance and maximizing between-class variance, this method effectively captures the intrinsic distribution structure of the data and reduces the potential influence of artificial classification on statistical results. In addition, the selection of the number of classes follows a trade-off between statistical stability and explanatory capability. An insufficient number of classes may obscure spatial heterogeneity and lead to an underestimation of factor explanatory power, whereas an excessive number of classes may result in inadequate sample sizes within certain categories, thereby causing instability in q-statistic estimation [35,36]. Considering the sample size and the distribution characteristics of the influencing factors, the data were classified into six classes in this study (Table 4), which ensures sufficient sample support for each category while adequately characterizing environmental gradient variations.

Table 3. Two-factor interaction.

Criteria for Judgment	Interaction Type
$q(X1 \cap X2) < \text{Min}(q1,q2)$	Nonlinear Weakening
$\text{Min}(q1,q2) < q(X1 \cap X2) < \text{Max}(q1,q2)$	Univariate Nonlinear Weakening
$q(X1 \cap X2) > \text{Max}(q1,q2)$	Bivariate Enhancement
$q(X1 \cap X2) = q1 + q2$	Independence
$q(X1 \cap X2) > q1 + q2$	Nonlinear Enhancement

Table 4. Indicators and classification of driving factors for landslide depth.

Dependent Variable (Y)	Independent Variable (X)	Factor	Unit	Number of Classes	Classification Method
Slip-surface depth (m)	X1	Elevation	m	6	Natural Breaks
	X2	Slope	°	6	Natural Breaks
	X3	Aspect	°	6	Natural Breaks
	X4	Vegetation coverage		6	Natural Breaks

4. Results

4.1. Two-Dimensional Surface Deformation Extraction

Based on the SBAS-InSAR technique, high-resolution ascending and descending deformation-rate fields from 2022 to 2024 were obtained for the study area. The results reveal pronounced spatial variability in surface deformation. The major deformation zones are concentrated on the middle to upper slopes along both sides of the valley, with descending-track deformation rates ranging from −1 to −196 mm/year (Figure 3a) and ascending-track rates from −1 to −106 mm/year (Figure 3b). Areas exhibiting large negative deformation are predominantly located on steep slopes with highly fractured rock masses, indicating that portions of the slope are undergoing persistent downslope movement or reactivation. Relatively stable areas are mainly distributed at the slope toes, terrace surfaces, and ridge zones, where deformation rates generally remain within ±20 mm/year.

Analysis of the eight representative landslides shows that Mashancun (03), Xishancun (02), Xiaoqicun (06 and 07), and Mengdonggou (08) exhibit continuous high negative deformation in both viewing geometries. Their sliding rates commonly reach −40 to −196 mm/year (descending) and −40 to −106 mm/year (ascending), with clearly defined deformation centers, distinct boundaries, and a spatial pattern of deformation attenuation from the center outward.

A detailed analysis of the annual LOS deformation rates from the descending track was conducted for each individual landslide. The results show clear differences in both the magnitude and spatial distribution of deformation among the landslides. For example,

the Xishancun, Sanzhaicun, and Mengdonggou landslides exhibit relatively large deformation magnitudes and strong activity, whereas the Xiaoqishan No. 02 landslide remains relatively stable overall.

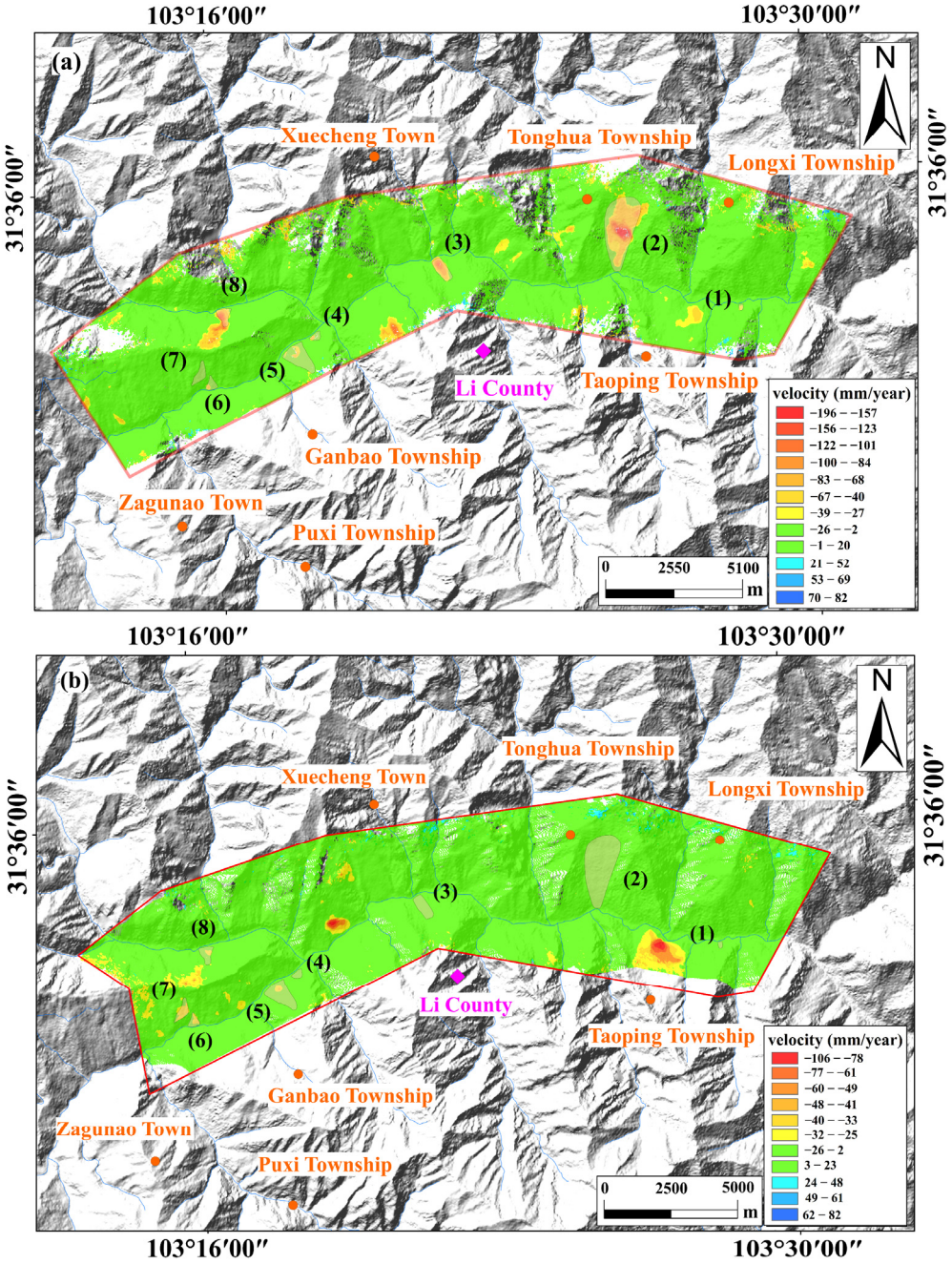


Figure 3. LOS deformation rates from ascending and descending tracks. (**a**) Descending-track LOS deformation rate map; (**b**) Ascending-track LOS deformation rate map. (numbers (1)–(8) indicate the locations of the eight representative landslides).

Specifically, the descending-track LOS deformation of the Taopingcun landslide ranges from −36 to −9 mm/year, with deformation mainly concentrated in the upper slope (Figure 4a). The Xishancun landslide shows deformation ranging from −195 to −13 mm/year, primarily in the mid-slope zone (Figure 4b). The Sanzhaicun landslide exhibits deformation between −108 and 2 mm/year, concentrated in the lower slope (Figure 4c). The Mashancun No. 01 landslide shows deformation ranging from −60 to 0 mm/year, concentrated on the right side of the slope toe (Figure 4d). The Mashancun

No. 02 landslide has deformation ranging from −44 to 7 mm/year, mainly in the lower slope area (Figure 4e). For the Xiaoqicun No. 01 landslide, deformation ranges from −46 to −1 mm/year and is concentrated on the left side of the slope toe (Figure 4f). The Xiaoqicun No. 02 landslide shows relatively small deformation (0–13 mm/year), primarily on the upper slope (Figure 4g). Finally, the Mengdonggou landslide exhibits deformation between −129 and −18 mm/year, with the most active zone located on the right side of the slope (Figure 4h).

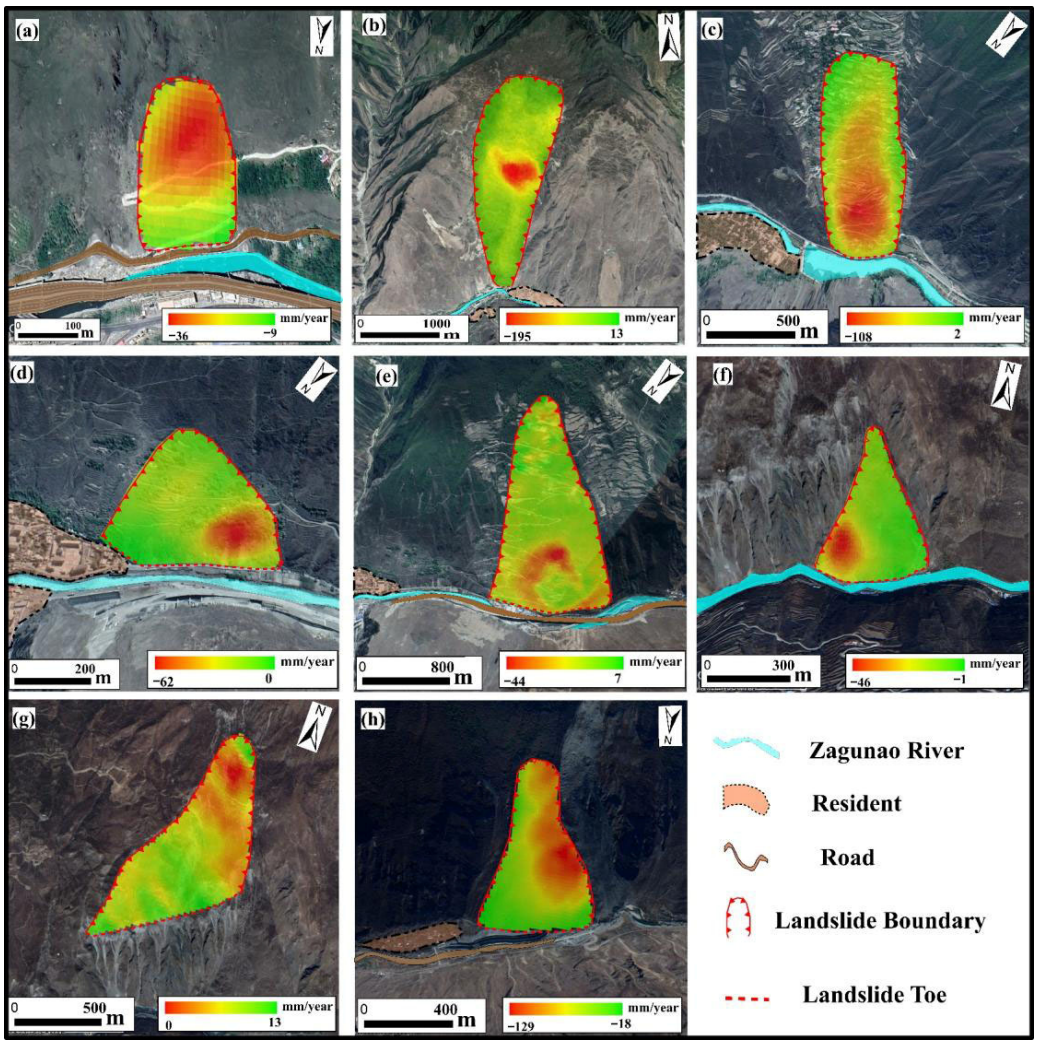


Figure 4. Detailed descending-track LOS deformation maps. (**a**) Taopingcun landslide; (**b**) Xishancun landslide; (**c**) Sanzhaicun landslide; (**d**) Mashancun No. 01 landslide; (**e**) Mashancun No. 02 landslide; (**f**) Xiaoqicun No. 01 landslide; (**g**) Xiaoqicun No. 02 landslide; (**h**) Mengdonggou landslide.

The ascending-track results reveal clear differences in both the magnitude and spatial distribution of LOS deformation across the landslides. These differences are reflected in the deformation-rate intervals and the locations of the primary deformation zones. Specifically, the Taopingcun landslide exhibits ascending-track deformation rates between −11 and −3 mm/year, with deformation mainly concentrated on the upper-left portion of the slope (Figure 5a). The Xishancun landslide shows deformation ranging from −17 to 23 mm/year, primarily in the lower slope area (Figure 5b). For the Sanzhaicun landslide, the deformation ranges from −14 to 13 mm/year and is mainly distributed in the middle to upper slope (Figure 5c).

The Mashancun No. 01 landslide displays deformation rates between −16 and 1 mm/year, concentrated in the upper slope zone (Figure 5d), while the Mashancun

No. 02 landslide has deformation rates between −56 and 20 mm/year, also concentrated in the lower slope (Figure 5e). The Xiaoqicun No. 01 landslide exhibits deformation between −30 and −8 mm/year, primarily on the right side of the slope (Figure 5f). The Xiaoqicun No. 02 landslide shows deformation between −22 and 5 mm/year, with deformation concentrated in the middle slope area (Figure 5g). Lastly, the Mengdonggou landslide presents deformation rates of −34 to 2 mm/year, with the main deformation zone located on the left side of the slope (Figure 5h).

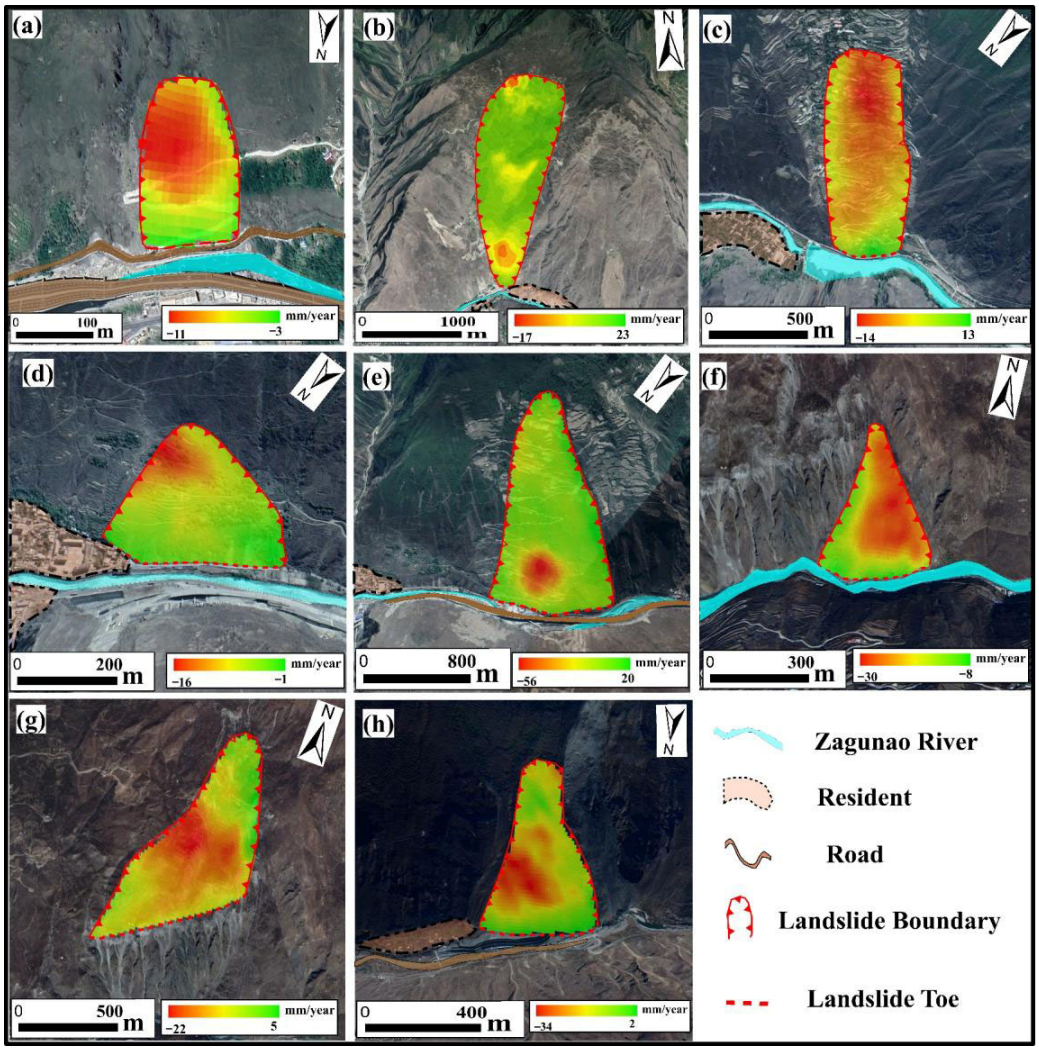


Figure 5. Detailed ascending-track LOS deformation maps. (**a**) Taopingcun landslide; (**b**) Xishancun landslide; (**c**) Sanzhaicun landslide; (**d**) Mashancun No. 01 landslide; (**e**) Mashancun No. 02 landslide; (**f**) Xiaoqicun No. 01 landslide; (**g**) Xiaoqicun No. 02 landslide; (**h**) Mengdonggou landslide.

By integrating satellite imaging parameters (incidence angle and azimuth angle) with slope and aspect information, a slope-based coordinate system was established to decompose the LOS deformation derived from SBAS-InSAR into slope-parallel and slope-normal components. The slope-parallel deformation results reveal that all landslides exhibit downslope displacement, although the magnitude and spatial distribution vary substantially among them. Overall, the high-value deformation zones are commonly located in the middle to upper parts of the slope, the slope toe, or the right flank of the slope.

For the Taopingcun landslide, the slope-parallel deformation ranges from 8 to 40 mm/year, directed downslope and mainly concentrated on the upper-right portion

of the slope (Figure 6a). The Xishancun landslide shows deformation rates between −26 and 545 mm/year, with deformation concentrated in the mid-slope area (Figure 6b). The Sanzhaicun landslide exhibits deformation ranging from 17 to 139 mm/year, primarily at the slope toe (Figure 6c). The Mashancun No. 01 landslide shows deformation between 0 and 96 mm/year, concentrated on the right side of the slope toe (Figure 6d). For the Mashancun No. 02 landslide, deformation ranges from 8 to 255 mm/year, with the most active zone located in the lower slope (Figure 6e). The Xiaoqicun No. 01 landslide exhibits deformation between 0 and 120 mm/year, mainly on the right side of the slope (Figure 6f). The Xiaoqicun No. 02 landslide shows rates ranging from −3 to 69 mm/year, concentrated in the mid-slope zone (Figure 6g). Finally, the Mengdonggou landslide displays deformation between 3 and 124 mm/year, with activity mainly concentrated on the right side of the slope (Figure 6h).

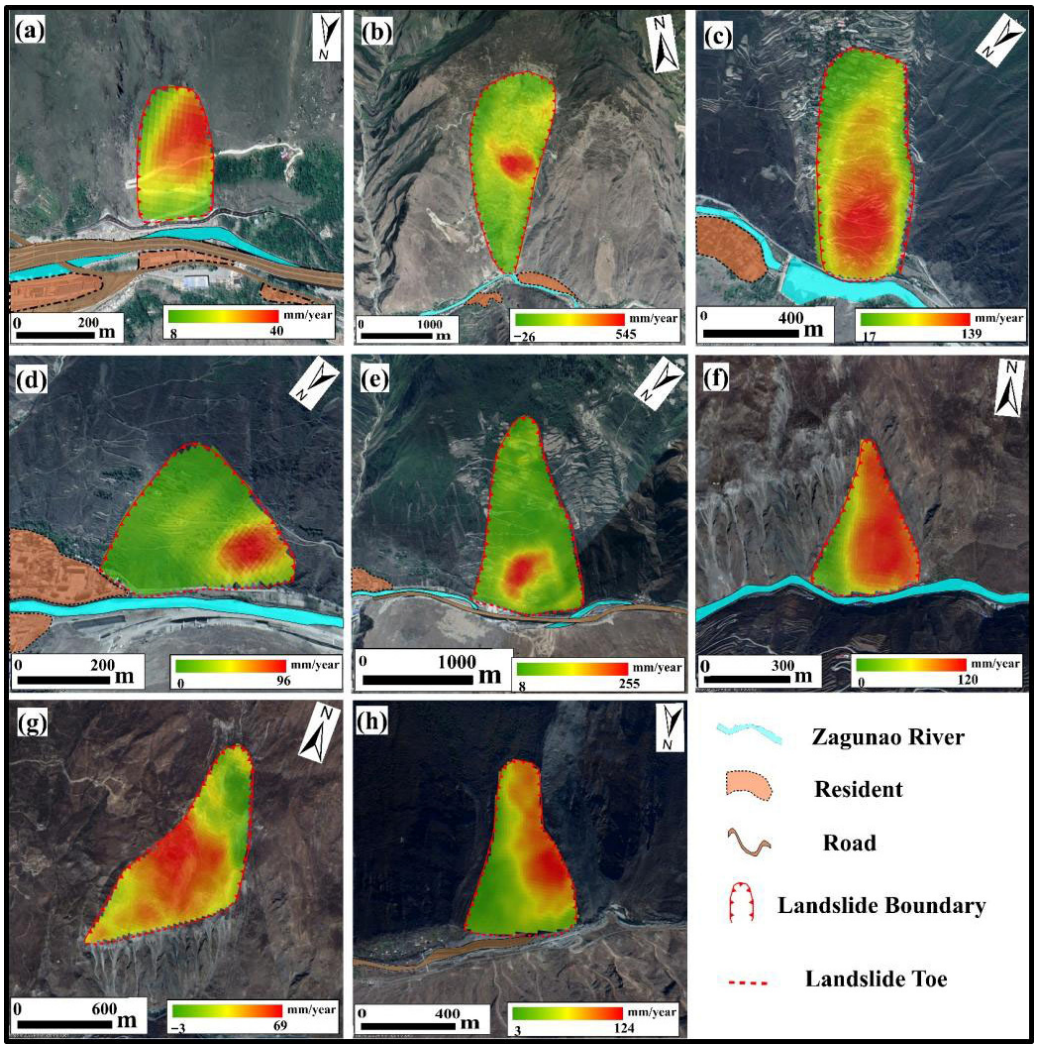


Figure 6. Detailed slope-parallel deformation maps. (**a**) Taopingcun landslide; (**b**) Xishancun landslide; (**c**) Sanzhaicun landslide; (**d**) Mashancun No. 01 landslide; (**e**) Mashancun No. 02 landslide; (**f**) Xiaoqicun No. 01 landslide; (**g**) Xiaoqicun No. 02 landslide; (**h**) Mengdonggou landslide.

The slope-normal deformation results show that the normal deformation rates of all landslides generally range from −6 to 254 mm/year. Among them, the Mashancun No. 02 landslide exhibits the highest normal deformation peak (254 mm/year), indicating strong activity in the normal direction as well. For most landslides, the peak normal deformation values fall within 30–120 mm/year. The locally observed negative values

(−26 to −6 mm/year) reflect minor compressive movements downslope but the overall trend is dominated by surface uplift or stress-release-related deformation.

For the Taopingcun landslide, the slope-normal deformation ranges from 10 to 28 mm/year, with upward displacement normal to the slope surface and deformation mainly concentrated in the middle-upper slope (Figure 7a). The Xishancun landslide exhibits a wide deformation range (−26 to 252 mm/year) and pronounced spatial heterogeneity, with deformation concentrated in the mid-lower slope. Localized high-value anomalies suggest the presence of strongly active sliding units within the landslide body (Figure 7b). The Sanzhaicun landslide shows relatively small normal deformation (3–59 mm/year), but deformation is clearly concentrated near the slope toe (Figure 7c).

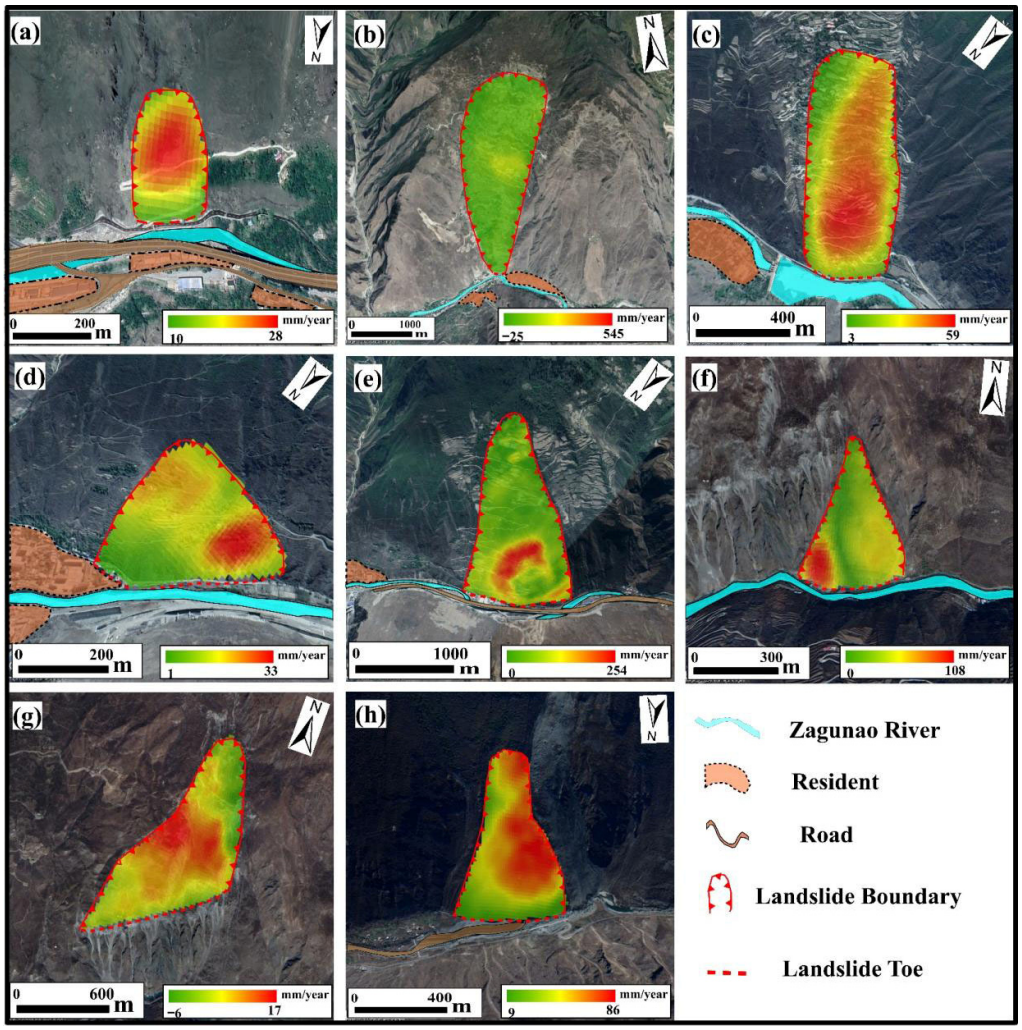


Figure 7. Detailed slope-normal deformation maps. (**a**) Taopingcun landslide; (**b**) Xishancun landslide; (**c**) Sanzhaicun landslide; (**d**) Mashancun No. 01 landslide; (**e**) Mashancun No. 02 landslide; (**f**) Xiaoqicun No. 01 landslide; (**g**) Xiaoqicun No. 02 landslide; (**h**) Mengdonggou landslide.

The Xiaoqicun No. 01 landslide presents deformation rates of 0–108 mm/year, mainly at the left side of the slope toe (Figure 7d). The Xiaoqicun No. 02 landslide displays deformation between −6 and 17 mm/year, with activity concentrated in the middle slope (Figure 7e). For the Mashancun No. 01 landslide, normal deformation ranges from 1 to 33 mm/year, with deformation concentrated in the lower slope, whereas the mid-upper slope remains relatively stable (Figure 7f). The Mashancun No. 02 landslide shows a large deformation range (0–254 mm/year), with the most active zone located in the lower slope, forming a clear contrast with the relatively stable rear edge of the landslide (Figure 7g).

The Mengdonggou landslide exhibits deformation between 9 and 86 mm/year, concentrated mainly on the right side of the slope and demonstrating strong spatial variability (Figure 7h).

4.2. Slip-Surface Depth Inversion

4.2.1. Analysis of Inversion Results

The inverted slip-surface depths reveal that all landslides exhibit pronouncedly irregular geometric features, with depth varying non-uniformly across the slope bodies and the locations of maximum depth differing from one landslide to another. The Taopingcun landslide has slip-surface depths of 16–50 m, with the maximum depth concentrated in the upper-right part of the slope (Figure 8a). The Xishancun landslide shows depths ranging from 1 to 98 m, with the deepest areas located on both sides of the lower slope (Figure 8b). For the Sanzhaicun landslide, depths range from 1 to 32 m, with the maximum depth occurring in the upper slope (Figure 8c). The Xiaoqicun No. 01 landslide has depths of 12–72 m, with the deepest zone concentrated on the lower-right portion of the slope (Figure 8d). The Xiaoqicun No. 02 landslide exhibits depths of 4–74 m, with the maximum depth located mainly in the mid-slope area (Figure 8e). The Mashancun No. 01 landslide shows depths of 4–54 m, with the deepest region on the lower-left slope (Figure 8f). The Mashancun No. 02 landslide has depths ranging from 1 to 45 m, with the maximum depth occurring in the upper slope (Figure 8g). The Mengdonggou landslide displays depths of 9–92 m, with the deepest zone concentrated on the lower-left slope (Figure 8h).

Overall, the slip-surface depths exhibit a wide range, from as shallow as 1 m (local areas of the Xishancun and Sanzhaicun landslides) to as deep as 98 m (Xishancun landslide), highlighting the strong spatial heterogeneity within the landslide bodies. The non-uniform distribution of slip-surface depth is closely related to slope geometry, slope-toe configuration, and landslide type, providing essential insight into overall slope stability and potential sliding trends.

A statistical analysis of the inverted thickness was conducted for eight representative landslides in the study area (Table 5). Under a unified grid resolution of 13.66 m, the optimal regularization parameter α for the individual landslides ranges from 10^{-3} to 10^{-1}, indicating that different landslides require different levels of smoothness constraint during thickness inversion. The results show that the maximum thickness (h_max) varies between 32.99 and 98.25 m, with the Xishancun and Mengdonggou landslides both exceeding 90 m, suggesting a relatively large overall scale. The mean thickness (h_mean) ranges from 15.51 to 47.26 m, whereas the 90th percentile thickness (h_90%) spans from 21.99 to 67.06 m and is consistently higher than the mean. Together, these statistical metrics characterize the degree of thickness concentration and spatial heterogeneity of the landslides, providing a robust quantitative basis for subsequent landslide scale assessment and comparative analysis of structural characteristics.

Table 5. Summary of inverted slip-surface depth statistics.

Landslide Name	Grid (m)	α	h_max (m)	h_90% (m)	h_mean (m)
Taopingcun Landslide	13.6573	10^{-1}	49.996267	39.583	26.936
Xishancun Landslide	13.6573	10^{-3}	98.246	63.728	47.258
Sanzhaicun Landslide	13.6573	10^{-3}	32.98654	21.989	15.51
Ma Mountain No. 1 Landslide	13.6573	10^{-2}	73	53.935	40.544
Ma Mountain No. 2 Landslide	13.6573	10^{-3}	73.985	50.986	37.29
Xiaoxi No. 1 Landslide	13.6573	10^{-3}	54	27.389	20.657
Xiaoxi No. 2 Landslide	13.6573	10^{-2}	45.011	38.299	25.656
Mengdonggou Landslide	13.6573	10^{-1}	91.979	67.06	35.719

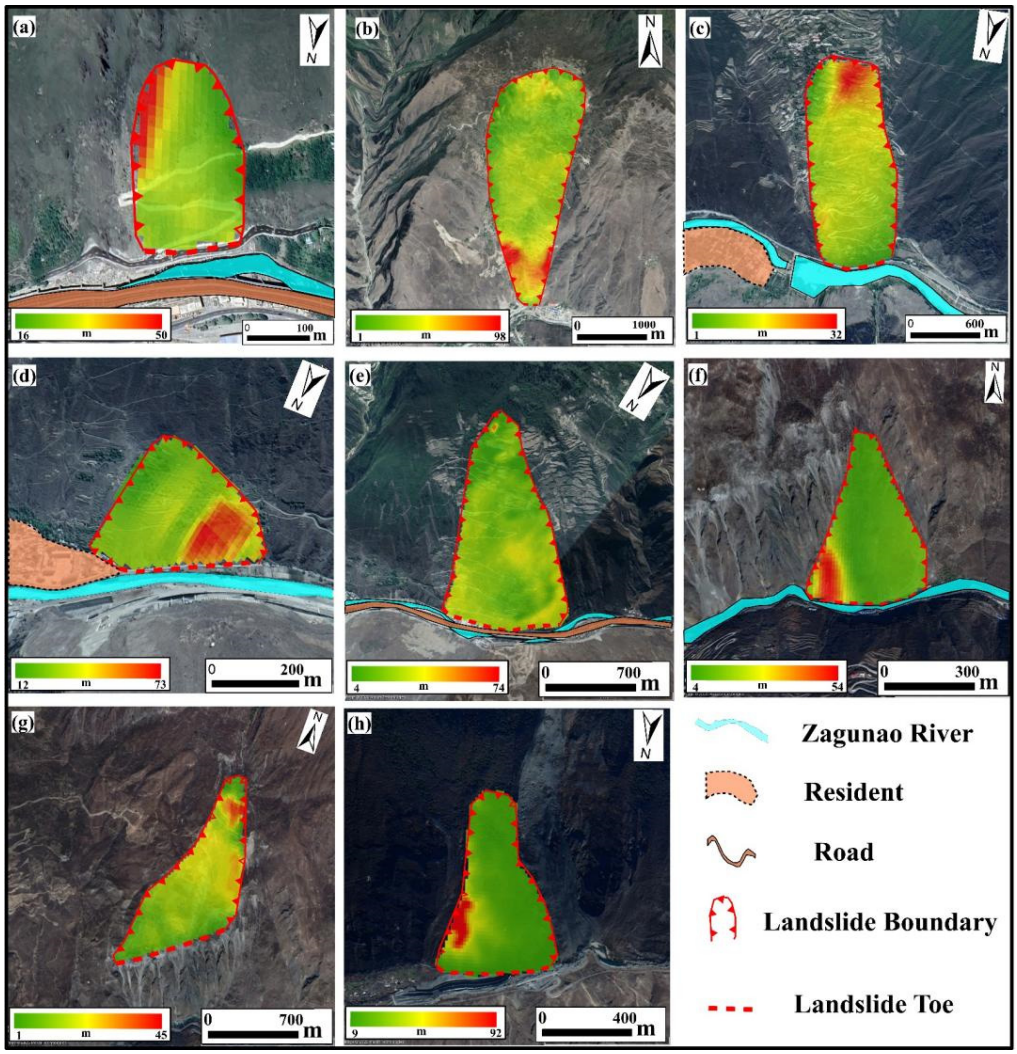


Figure 8. Slip-surface depth distribution maps. (**a**) Taopingcun landslide; (**b**) Xishancun landslide; (**c**) Sanzhaicun landslide; (**d**) Mashancun No. 01 landslide; (**e**) Mashancun No. 02 landslide; (**f**) Xiaoqicun No. 01 landslide; (**g**) Xiaoqicun No. 02 landslide; (**h**) Mengdonggou landslide.

4.2.2. Validation of Inversion Results

This study obtained detailed borehole profile data for only four landslides—Xishancun, Sanzhaicun, Mashan Village No. 01, and Mashan Village No. 02. Therefore, the sliding-surface depths of these four landslides were validated to assess the accuracy of the inversion method. The specific validation results are as follows:

For the Xishancun landslide, the slip-surface depth was compared with cross-sectional profiles derived from borehole investigations reported by Luo (2015) and Ma (2016) [37,38]. The comparison shows that the inverted depth and the borehole-based interpretation exhibit generally consistent overall trends, although noticeable discrepancies occur near an elevation of approximately 2400 m (Figure 9a,b). Validation data for the Sanzhaicun landslide and the Mashancun No. 01 and No. 02 landslides were extracted from the exploratory profiles presented in the Fine Investigation Report on High-Altitude Geological Hazards in the Alpine Canyon Region of Sichuan Province, compiled by the Guanghan Geological Engineering Exploration Institute of Sichuan Province. The comparison demonstrates good agreement between the inverted slip-surface depths and the geological profiles in terms of overall geometric characteristics (Figure 9c–e). Local discrepancies are observed in the elevation range of 1620–1680 m for the Sanzhaicun landslide, around 1600–1620 m for the

Mashancun No. 01 landslide, and within 1600–1700 m for the Mashancun No. 02 landslide, where the differences are relatively more pronounced.

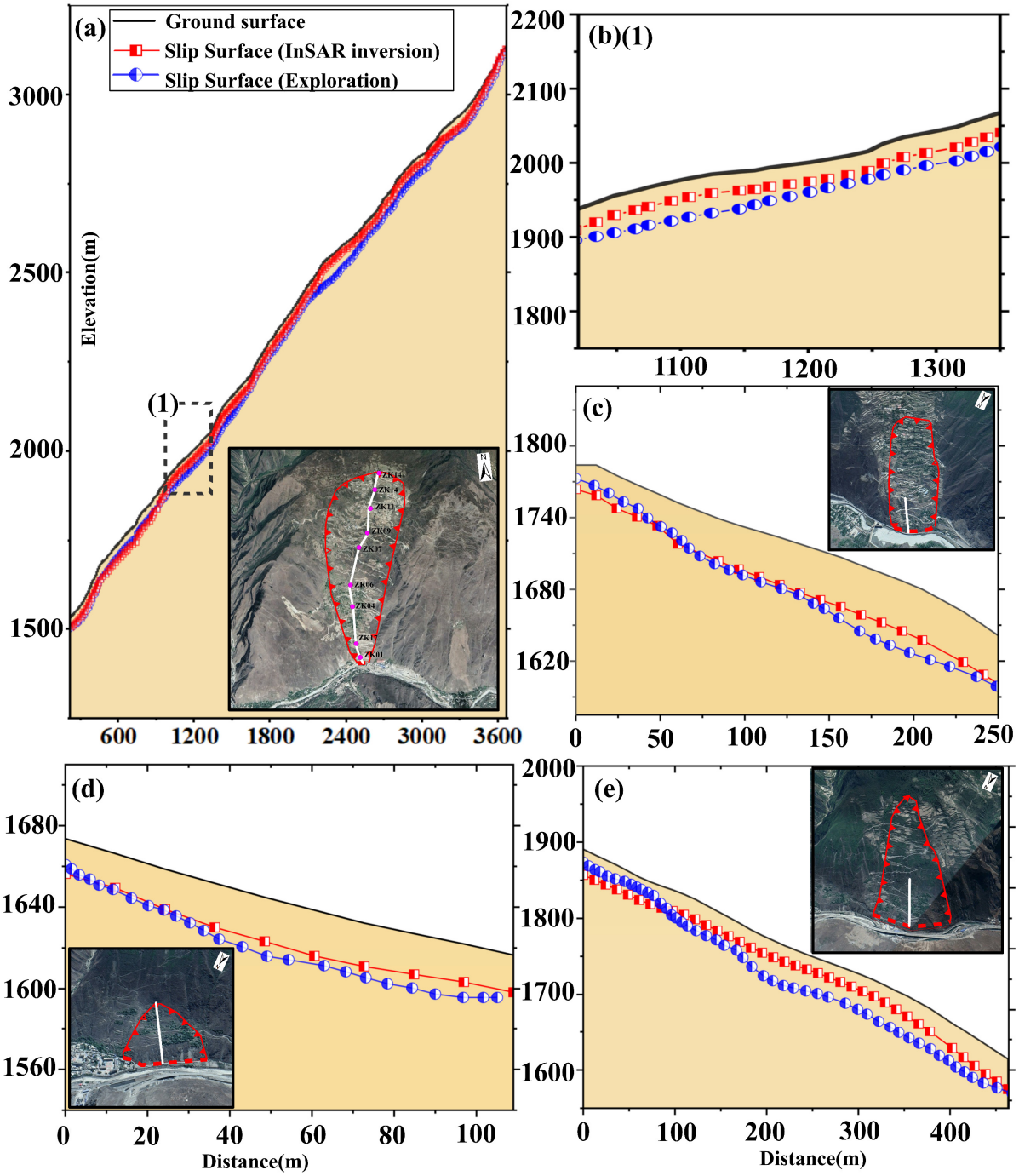


Figure 9. Slip-surface profile validation. (**a**) Xishancun landslide slip-surface profile validation; (**b**) Local slip-surface profile validation for the Xishancun landslide; (**c**) Sanzhaicun landslide slip-surface profile validation; (**d**) Mashancun No. 01 landslide slip-surface profile validation; (**e**) Mashancun No. 02 landslide slip-surface profile validation.

The reliability of the sliding surface depth results for four different landslides was quantitatively evaluated using three key statistical metrics: Root Mean Square Error (RMSE), Coefficient of Determination (R^2), and Correlation Coefficient (Table 6).

Overall, all four landslides have R^2 values above 0.92 and correlation coefficients above 0.97, suggesting that the sliding surface depths inverted by the two methods exhibit

extremely strong explanatory power and correlation. However, there are noticeable differences in the Root Mean Square Error. The Sanzhaicun and Mashancun 01 landslides have relatively low RMSE values, while the Xishancun and Mashancun 02 landslides show higher RMSE values.

Table 6. Slip-surface depth verification table.

Landslides	RMSE/m	Relative Uncertainty	R^2	Correlation Coefficient
Xishancun landslide	±16.5613	16%	0.9878	0.9748
Sanzhaicun landslide	±4.9558	15%	0.9226	0.9961
Mashangcun No. 01 Landslide	±8.9025	10%	0.9645	0.9951
Mashangcun No. 02 Landslide	±15.7550	20%	0.9321	0.989

Due to the lack of accessible geological investigations, borehole data, or cross-sectional profiles for the remaining landslides in the study area, direct validation of all inversion results could not be performed. However, for the four landslides with available independent validation data, the inverted results show high consistency with the observed data in terms of R^2, correlation coefficients, and RMSE, indicating that the proposed method exhibits good reliability and stability.

4.3. Analysis of Factors Influencing Slip-Surface Depth

4.3.1. Single-Factor Detection

The univariate detection evaluates the explanatory power of each driving factor on the spatial variation in landslide depth using the q-statistic. The q values obtained in this study represent the relative explanatory power of each factor for the spatial variability of slip-surface depth at the scale considered in this research, and their magnitudes do not indicate absolute controlling strength that is directly comparable across different spatial scales. The applicability of these conclusions at other scales therefore requires further verification. The *p*-value indicates whether the explanatory power is statistically significant. Generally, when $p > 0.05$, the corresponding q-value is considered unreliable. In this study, all *p*-values are less than 0.05, indicating that the q-values are statistically significant and that the four selected factors provide strong explanatory power for the spatial distribution of slip-surface depth.

For the Xishancun, Sanzhaicun, Mashancun No. 1, and Mashancun No. 2 landslides, elevation is identified as the primary controlling factor, with q-statistics of 0.127, 0.378, 0.274, and 0.381, respectively. This indicates that elevation independently explains 12.7% to 42.6% of the spatial variation in slip-surface depth (Figure 10). For the Xiaoqi No. 1 and Mengdonggou landslides, slope aspect is the dominant factor, with q-values of 0.309 and 0.455, respectively, suggesting that aspect independently explains 30% to 45% of the spatial variability in slip-surface depth (Figure 10).

Overall, elevation exhibits the strongest explanatory power, indicating that the distribution of slip-surface depth has a clear spatial correlation with elevation (Table 7). Slope aspect provides the second strongest explanatory effect, also influencing the spatial pattern of depth to a certain extent.

The GeoDetector results in this study indicate that elevation is the dominant controlling factor of slip-surface depth. This is primarily attributed to the fact that, in high mountain-gorge terrain, slopes are subjected to substantial gravitational potential energy. According to slope stress-distribution theory, steep slopes must develop potential shear zones at greater depths to counterbalance the large downslope driving forces by mobilizing sufficient resisting strength. Meanwhile, intense river incision in Li has caused significant unloading on high-elevation slopes, generating tensile fractures in the deep rock

mass. These fractures not only provide weak structural planes conducive to slip-surface formation but also enhance groundwater infiltration, further softening the deep-seated materials. Consequently, elevation governs the lower bound of slip-surface depth by jointly influencing the slope's stress state, unloading history, and deep hydrological processes.

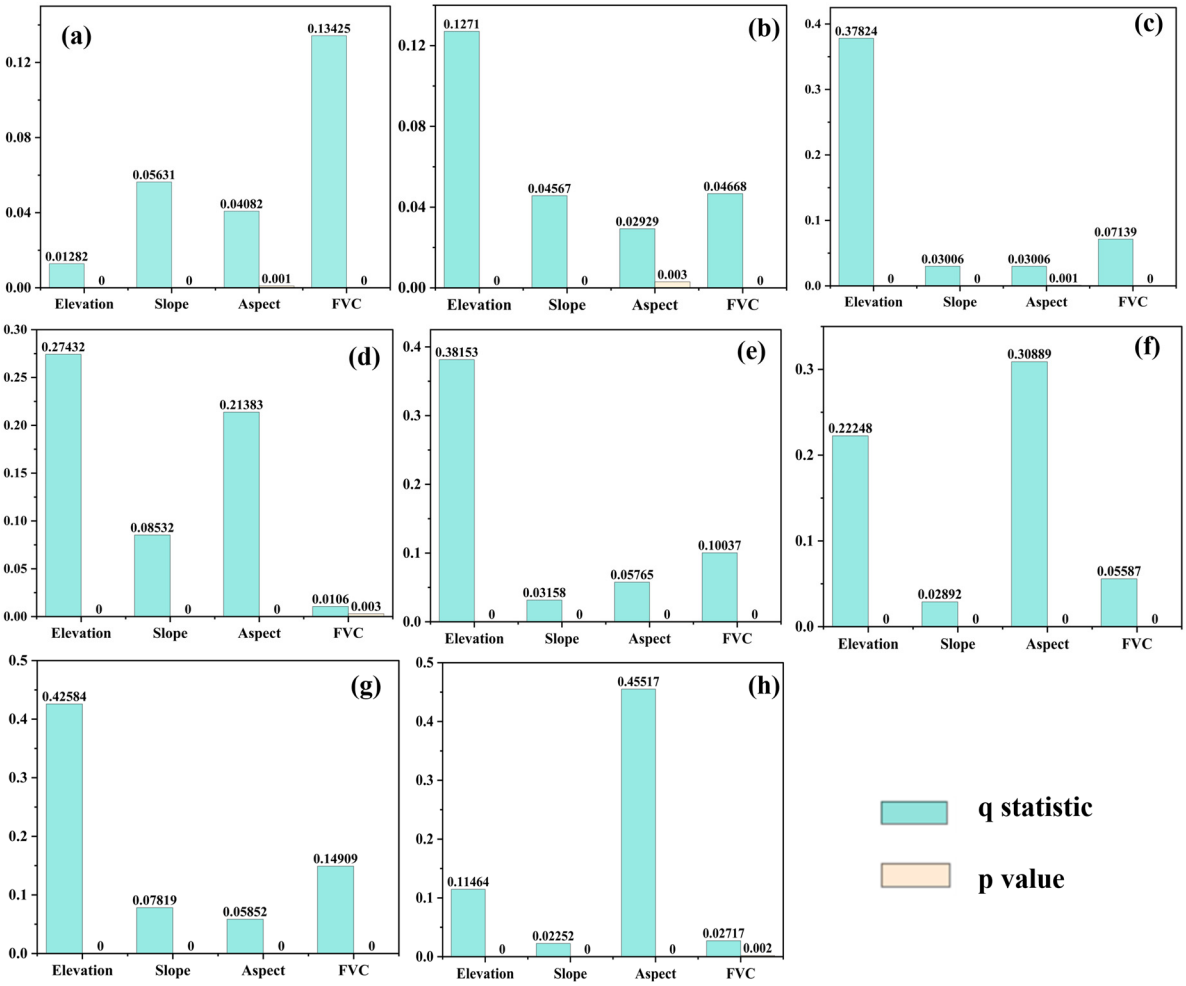


Figure 10. Univariate factor-detection results. (**a**) Taopingcun landslide; (**b**) Xishancun landslide; (**c**) Sanzhaicun landslide; (**d**) Mashancun No. 01 landslide; (**e**) Mashancun No. 02 landslide; (**f**) Xiaoqicun No. 01 landslide; (**g**) Xiaoqicun No. 02 landslide; (**h**) Mengdonggou landslide.

Table 7. Q-statistics of single factors for each landslide.

No.	Landslide Name	Primary Controlling Factor	q Statistic
1	Taopingcun Landslide	FVC	0.134
2	Xishancun Landslide	Elevation	0.127
3	Sanzhaicun Landslide	Elevation	0.378
4	Mashancun No. 1 Landslide	Elevation	0.274
5	Mashancun No. 2 Landslide	Elevation	0.381
6	Xiaoqicun No. 1 Landslide	Aspect	0.309
7	Xiaoqicun No. 2 Landslide	Elevation	0.426
8	Mengdonggou Landslide	Aspect	0.455

4.3.2. Interaction Factor Detection

Interaction detection is used to assess how the combined effect of two driving factors alters their explanatory power for landslide depth—whether the interaction enhances, weakens, or remains independent of the individual factors. When the q-value of a factor

pair exceeds that of either single factor, the interaction is considered enhanced. Interaction types include nonlinear enhancement, bivariate enhancement, independence, univariate nonlinear weakening, and nonlinear weakening, among which nonlinear enhancement and nonlinear weakening represent the strongest effects.

As shown in Figure 11, the interaction detection of the four driving factors across the study area exhibits two types of outcomes: nonlinear enhancement and bivariate enhancement. This indicates that all factor pairs produce stronger explanatory power for landslide depth than any single factor, suggesting that slip-surface depth is jointly controlled by multiple factors working in a synergistic manner. Therefore, the interrelationships among the influencing factors should be considered, as their combined effects play an important role in shaping the spatial distribution of landslide depth.

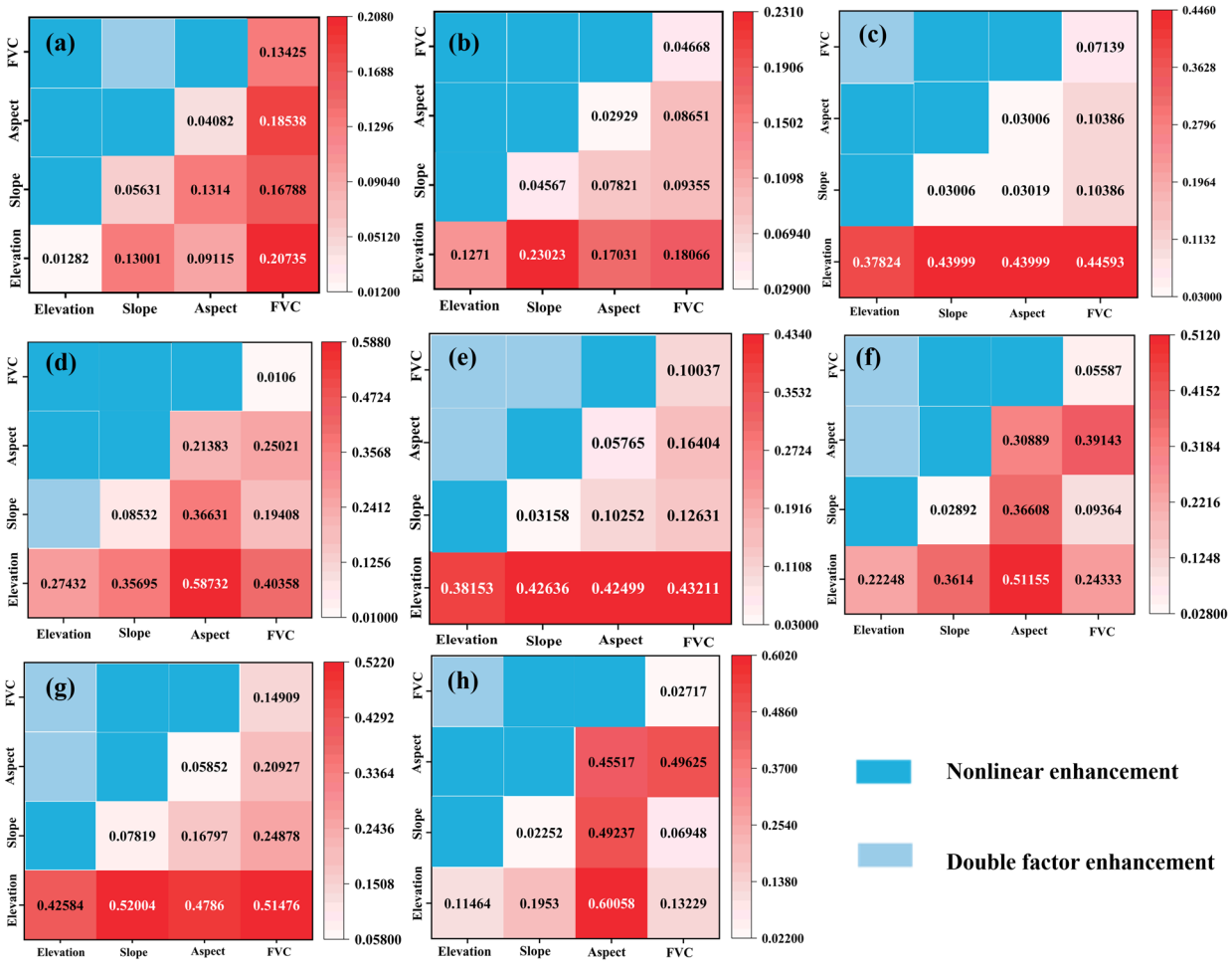


Figure 11. Interaction factor detection. (**a**) Taopingcun landslide; (**b**) Xishancun landslide; (**c**) Sanzhaicun landslide; (**d**) Mashancun No. 01 landslide; (**e**) Mashancun No. 02 landslide; (**f**) Xiaoqicun No. 01 landslide; (**g**) Xiaoqicun No. 02 landslide; (**h**) Mengdonggou landslide.

Figure 11 presents interaction-detection heatmaps for the four factors—elevation, slope, aspect, and fractional vegetation cover (FVC)—across the eight creep-type landslides (a–h). The results reveal significant spatial heterogeneity in the interaction strength between landslide depth and the influencing factors. Overall, the interaction between elevation and slope is the most prominent (nonlinear enhancement). For example, the elevation–slope interaction reaches 0.35695 in the Mashancun No. 01 landslide (Figure 11d), 0.42636 in the Mashancun No. 02 landslide (Figure 11e), and 0.36 in the Xiaoqicun No. 01 landslide (Figure 11f). In the Xiaoqicun No. 02 and Mengdonggou landslides, the interaction values

reach approximately 0.52004 and 0.60088, respectively (Figure 11g,h), appearing as dark red regions—among the highest values in each subplot—indicating that elevation and slope jointly provide the strongest explanatory power for slip-surface depth.

The second strongest interaction is elevation × aspect, with values of 0.38732 in the Mashancun No. 01 landslide (Figure 11d) and 0.39143 in the Xiaoqicun No. 01 landslide (Figure 11e). In contrast, the interaction strength between FVC and other factors is generally low—mostly within 0.01–0.25 (e.g., FVC × elevation in the Taopingcun landslide is only 0.01282, and FVC × slope in the Xishancun landslide is about 0.09355)—indicating a relatively weak joint explanatory effect.

Based on the above analysis of the influencing factor, the dominant controls on slip-surface depth and the strength of their interactions vary significantly among the landslides, indicating that the deep-seated structure and deformation mechanisms are highly dependent on local topographic conditions. Meanwhile, the interaction effects among factors are generally stronger than the explanatory power of any single factor, further demonstrating that creep-type landslides are governed by multi-factor coupling. This highlights the pronounced multi-scale variability and spatial heterogeneity inherent in their controlling mechanisms.

4.4. Statistical Analysis of Sliding-Surface Depth Characteristics

This study quantitatively analyzes the statistical relationships between slip-surface depth and topographic factors. By integrating boxplots with trend-line analysis, the concentration ranges, dispersion patterns, and overall variation trends of slip-surface depth with elevation and slope can be clearly identified. This provides a reliable statistical basis for interpreting the formation of slip-surface depth, identifying controlling factors, and inferring deep-seated sliding structures, thereby revealing the response characteristics of landslide internal geometry under different topographic conditions.

The boxplots of slip-surface depth versus elevation indicate three typical patterns:

(1) Curved type: depth shows an "upper-thin-middle-thick-lower-thin" curved pattern, corresponding to a concave, rotational slip surface. (2) Descending type: depth increases linearly with decreasing elevation, showing "thin at the crest and thick at the toe", corresponding to a nearly planar slip surface. (3) Ascending type: depth decreases linearly with decreasing elevation, showing "thick at the crest and thin at the toe", also corresponding to a near-planar slip surface.

Because the eight selected typical landslides share the same bedrock conditions and all exhibit homogeneous soil-like material properties, their classification can be aligned with geological criteria based on sliding-surface morphology [39,40]. The three characteristic patterns observed in the variation in sliding-surface depth with elevation correspond well to rotational landslides, push-type translational landslides, and traction-type translational landslides. Therefore, the eight landslides were grouped into these three categories—rotational, push-type translational, and traction-type translational—for subsequent discussion and analysis. This study establishes a conceptual correspondence between the statistical characteristics of slip-surface geometry and classical landslide mechanical models to provide physical interpretations of deformation patterns for different landslide types, thereby helping to explain the plausibility of the statistical classification results within the framework of classical landslide mechanics.

(1) Rotational landslides

The Taopingcun, Xiaoqicun No. 2, and Mengdonggou landslides are identified as typical rotational landslides, with arc-shaped slip surfaces and maximum slip-surface depth located in the mid-slope region (Figure 12). For the Taopingcun landslide, the greatest depth occurs at elevations of 1575–1715 m and slopes of 15–30°, consistent with an average

slope angle of approximately 20° (Figure 12a,a1,a2). The Xiaoqicun No. 2 landslide exhibits maximum depth at elevations of 2025–2225 m and slopes of 10–20° (Figure 12b,b1,b2)). The Mengdonggou landslide also shows a thickened mid-slope zone at elevations of 1725–1825 m and slopes of 27–32° (Figure 12c,c1,c2).

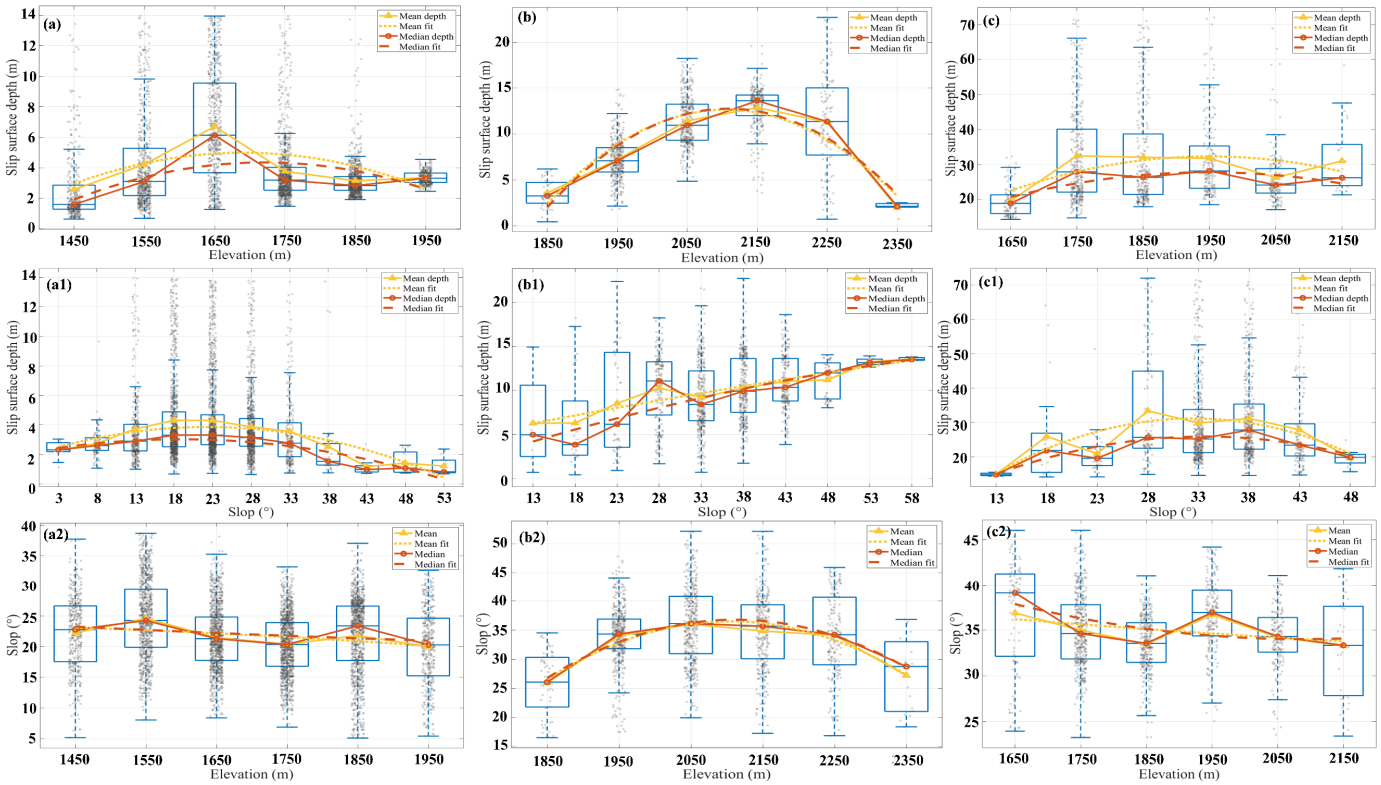


Figure 12. Statistical relationships among slip-surface depth, elevation, and slope. (**a**) Slip-surface depth vs. elevation for the Taopingcun landslide; (**b**) Slip-surface depth vs. elevation for the Xiaoqicun No. 2 landslide; (**c**) Slip-surface depth vs. elevation for the Mengdonggou landslide; (**a1**) Slip-surface depth vs. slope for the Taopingcun landslide; (**b1**) Slip-surface depth vs. slope for the Xiaoqicun No. 2 landslide; (**c1**) Slip-surface depth vs. slope for the Mengdonggou landslide; (**a2**) Slope vs. elevation for the Taopingcun landslide; (**b2**) Slope vs. elevation for the Xiaoqicun No. 2 landslide; (**c2**) Slope vs. elevation for the Mengdonggou landslide.

These landslides share consistent geometric and mechanical characteristics. The mid-slope region acts as the main shear zone, where shear strain localizes and material strength deteriorates most significantly. Both the rear and frontal edges of the slip surface become notably thinner, forming a typical three-part deformation pattern characterized by tensile deformation at the crown, concentrated shear in the middle, and compressional deformation toward the toe. This further demonstrates that the spatial distribution of slip-surface depth is strongly controlled by topographic factors such as elevation and slope.

(2) Push-type translational landslides

The Xishancun, Mashancun No. 1, Mashancun. 2, and Xiaoqicun No. 1 landslides are classified as push-type translational landslides. Their slip surfaces are nearly planar, with relatively large depths concentrated near the slope toe where colluvial and accumulated materials are present (Figure 13). Specifically, the Xishancun landslide shows a deep slip surface at elevations of 1500–1700 m, reaching approximately 60 m below the ground surface (Figure 13a). A second deepened segment of the Mashancun No. 1 landslide occurs between elevations of 1570 and 1610 m, with a slip-surface depth of about 45 m (Figure 13b). The Mashancun No. 2 landslide exhibits its maximum slip-surface depth in the elevation range of 1550–1950 m, reaching nearly 60 m below the surface (Figure 13c). For the Xiaoqi-

cun No. 1 landslide, the deepest part of the slip surface appears between 1575 and 1675 m, also reaching approximately 60 m beneath the ground surface (Figure 13d).

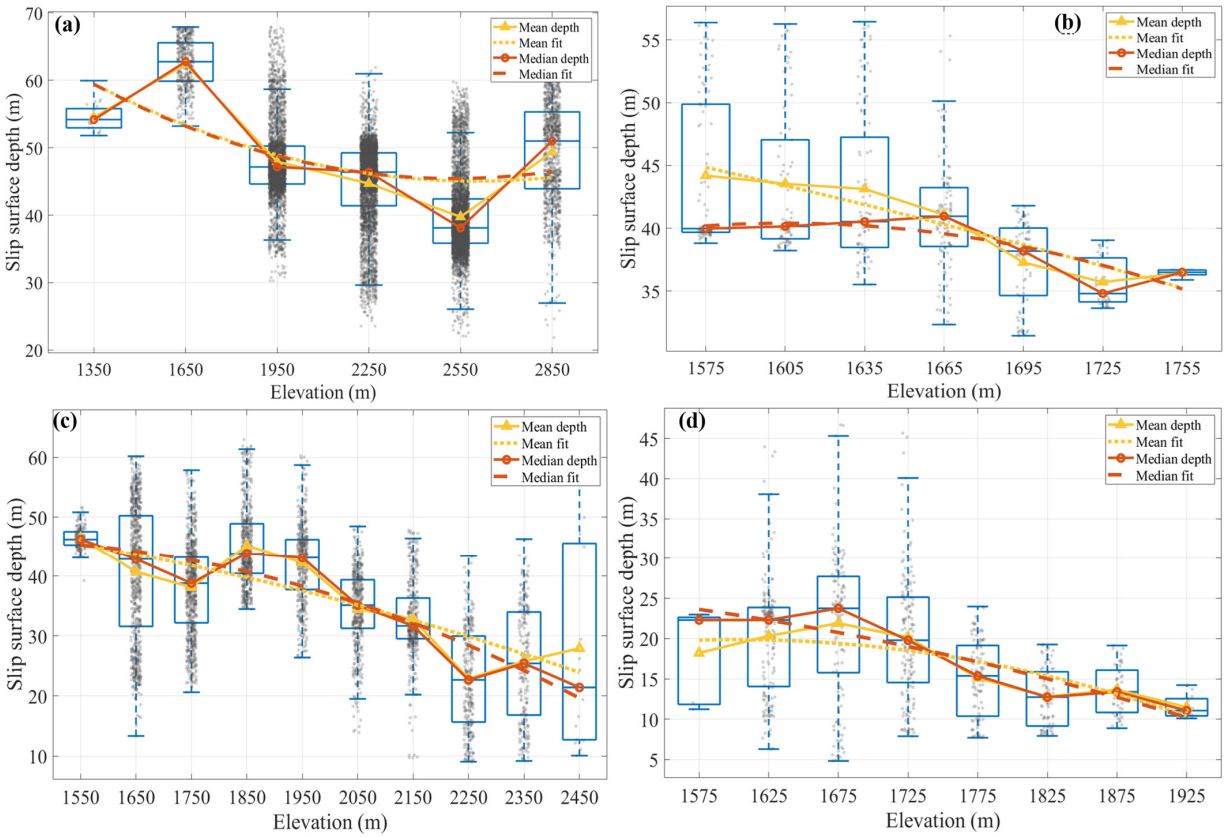


Figure 13. Statistical relationship between slip-surface depth and elevation. (**a**) Slip-surface depth vs. elevation for the Xishancun landslide; (**b**) Slip-surface depth vs. elevation for the Mashancun No. 1 landslide; (**c**) Slip-surface depth vs. elevation for the Mashancun No. 2 landslide; (**d**) Slip-surface depth vs. elevation for the Xiaoqicun No. 1 landslide.

Analysis of the boxplots showing the relationship between slip-surface depth and slope angle reveals that the Xishancun, Mashancun No. 1, Mashancun No. 2, and Xiaoqicun No. 1 landslides all exhibit greater slip-surface depths at slopes of approximately 40°, a condition favorable for material accumulation (Figure 14). For the Xishancun landslide, slip-surface depth increases progressively from low to moderate slope angles and reaches a peak at around 37–42° (Figure 14a). The Mashancun No. 1 landslide shows relatively small overall variation, but a similar thickening occurs near 37° (Figure 14b). The Mashancun No. 2 landslide exhibits thinning in the low-moderate slope range, followed by renewed thickening around 37–42° (Figure 14c). Although the Xiaoqicun No. 1 landslide has a generally thinner sliding mass, a slight increase in depth is still observed at moderate-high slope angles (Figure 14d).

These results indicate that a slope angle of approximately 40° represents a common threshold zone where slip-surface thickening occurs across all four landslides, highlighting a consistent sensitivity and control of slip-surface depth to slope angle.

Analysis of the boxplots of slope versus elevation reveals notable differences in slope distribution across the four landslides. For the Xishancun landslide (Figure 15a), slope angles generally decrease with increasing elevation: steep slopes dominate the lower elevations (around 1500 m), while higher elevations (around 2900 m) are relatively gentle. The Mashancun No. 1 landslide (Figure 15b) shows a pronounced steep segment at approximately 1605 m, after which the slope gradually decreases with increasing elevation.

In the Mashancun No. 2 landslide (Figure 15c), slope angles rise rapidly from 1575 m to about 1675 m, remain high within the mid-elevation range of 1675–1825 m, and then slightly decrease at higher elevations. The Xiaoqicun No. 1 landslide (Figure 15d) exhibits increasing slope angles from 1550 m to 1850 m, reaching a maximum near 1850 m before gradually flattening.

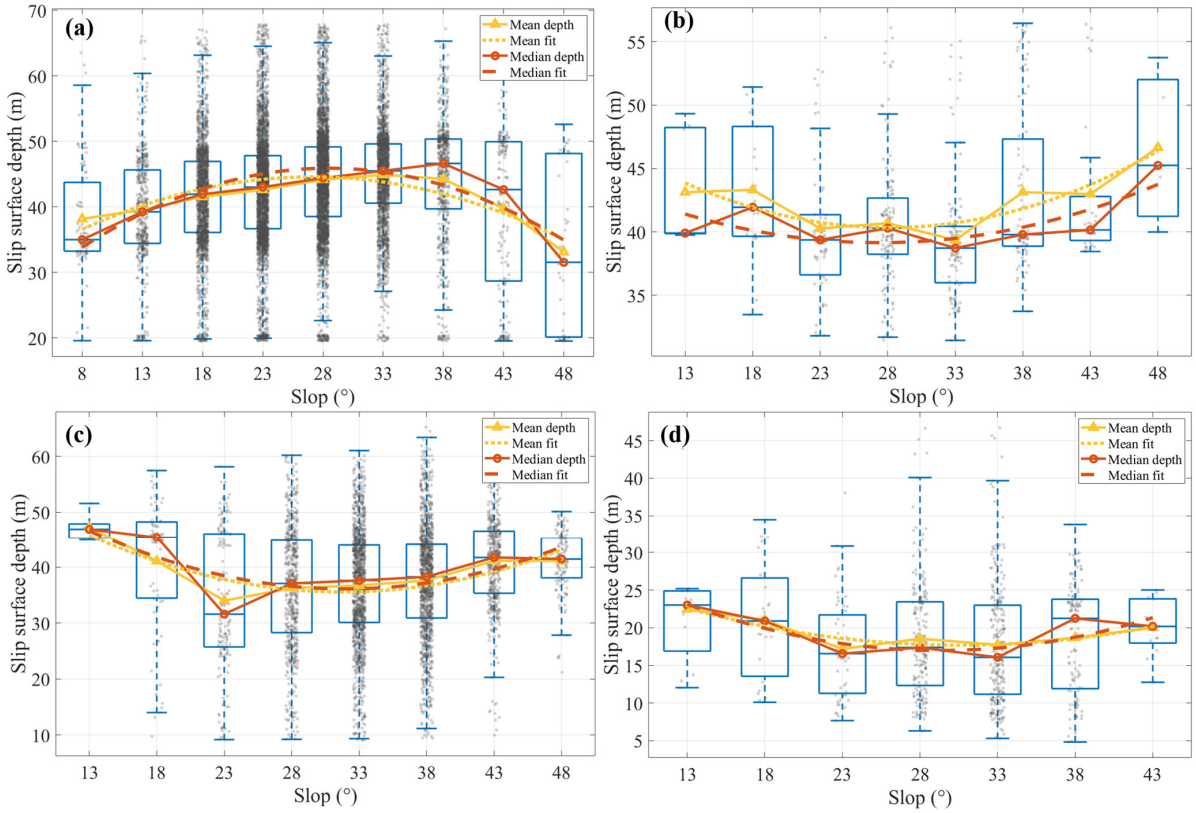


Figure 14. Statistical relationship between slip-surface depth and slope. (**a**) Slip-surface depth vs. slope for the Xishancun landslide; (**b**) Slip-surface depth vs. slope for the Mashancun No. 1 landslide; (**c**) Slip-surface depth vs. slope for the Mashancun No. 2 landslide; (**d**) Slip-surface depth vs. slope for the Xiaoqicun No. 1 landslide.

Overall, most landslides display distinct local slope peaks within specific mid-elevation bands, although the detailed evolutionary trends differ among them.

(3) Traction-type translational landslide

The Sanzhaicun landslide is a typical traction-type translational landslide, characterized by a nearly planar slip surface and overall displacement along a shallow weak layer induced by the traction exerted from the upper strata. The statistical relationships reveal that slip-surface depth increases significantly with elevation (Figure 16a): within the elevation range of 1525–1925 m, the depth increases from approximately 12 m to more than 20 m, indicating that the upper slope (crest zone) forms the deepest and most strongly accumulated portion of the landslide mass.

The relationship between slip-surface depth and slope (Figure 16b) shows rapid thickening within the slope range of 7.5–17.5°, followed by a gentle increase at higher slope angles. In addition, the elevation–slope relationship (Figure 16c) indicates that slope angles slightly decrease with increasing elevation; the gentler slopes at higher elevations promote material accumulation in the upper slope, which in turn deepens the slip surface. Overall, the Sanzhaicun landslide displays the typical characteristics of a traction-type translational landslide, with the deepest slip surface located in the gentle upper-slope region and progressively shallower depths downslope.

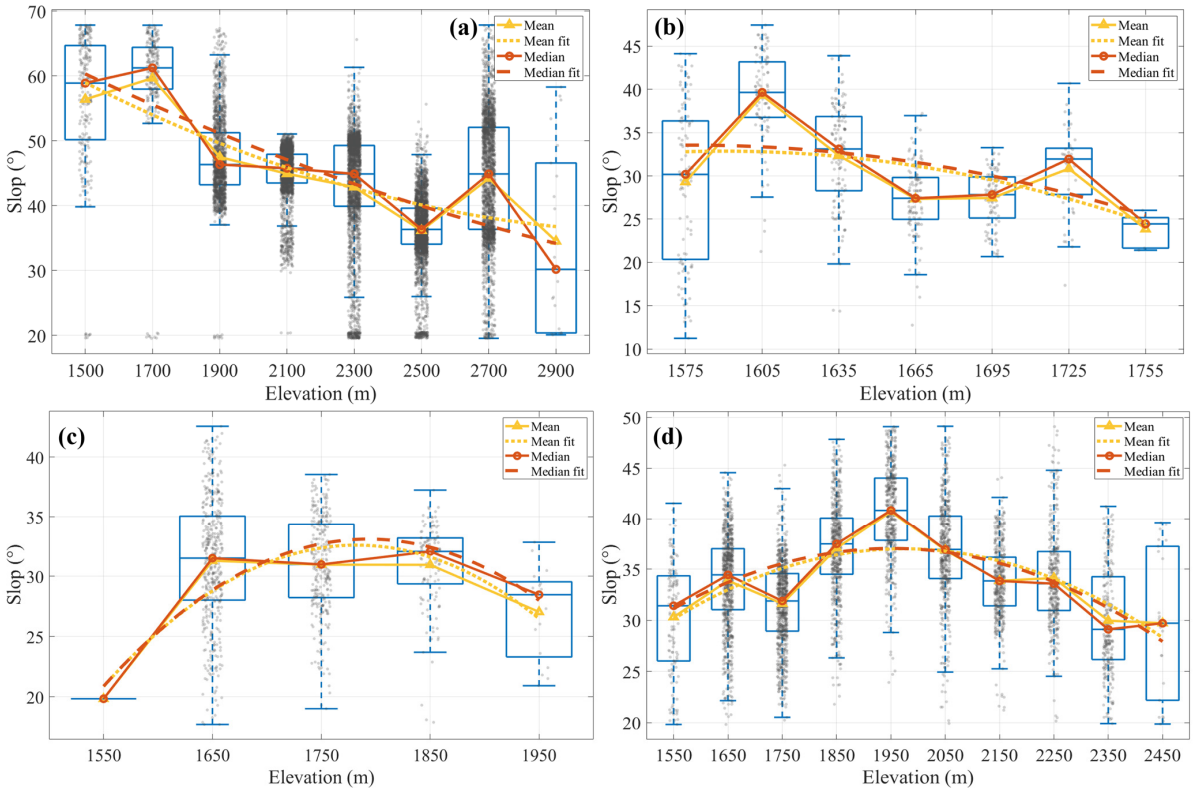


Figure 15. Statistical relationship between elevation and slope for the landslides. (**a**) Elevation vs. slope for the Xishancun landslide; (**b**) Elevation vs. slope for the Mashancun No. 1 landslide; (**c**) Elevation vs. slope for the Mashancun No. 2 landslide; (**d**) Elevation vs. slope for the Xiaoqicun No. 1 landslide.

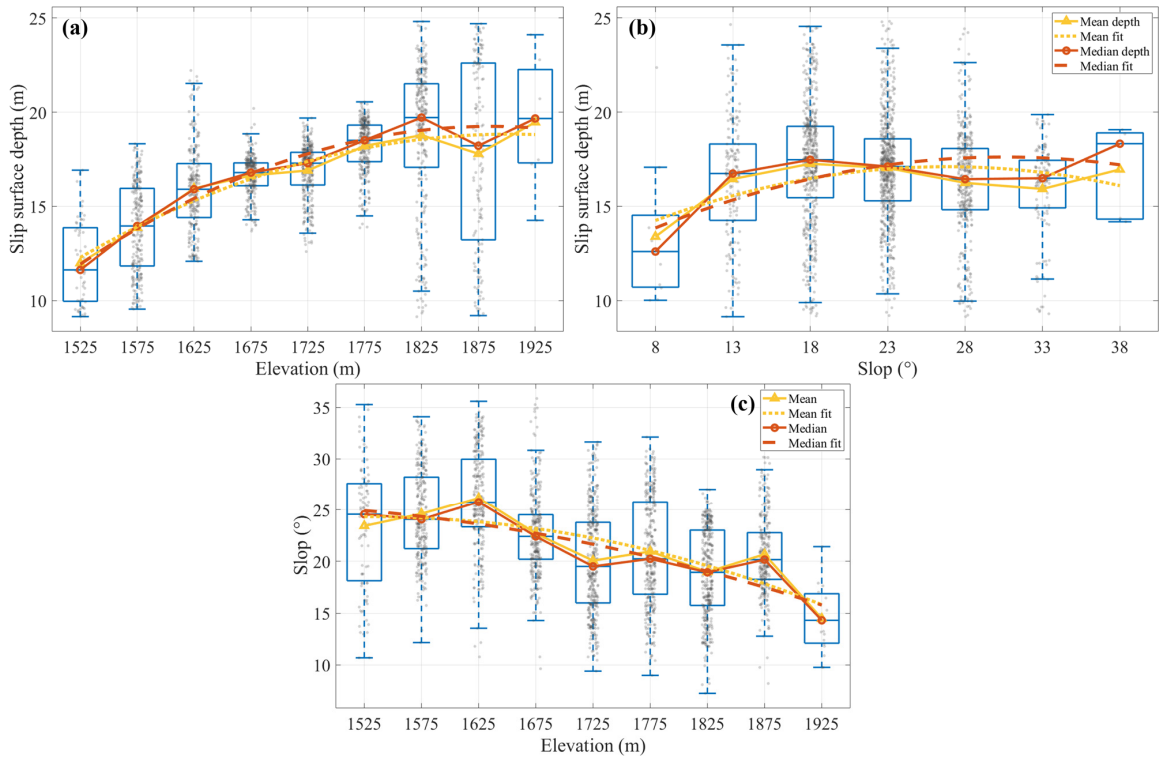


Figure 16. Statistical relationships among slip-surface depth, elevation, and slope for the Sanzhaicun landslide. (**a**) Slip-surface depth vs. elevation; (**b**) Slip-surface depth vs. slope; (**c**) Elevation vs. slope.

The landslide classification proposed in this study is based on the statistical characteristics of slip-surface geometry. It is primarily intended to characterize the statistical differences in slip-surface morphology and its relationship with topographic position among different landslides, thereby providing a structured diagnostic perspective for identifying their potential deformation modes and evolutionary characteristics.

5. Discussion

5.1. Discussion on the Reliability and Applicability of the Slip-Surface Depth Inversion Method

The inversion of slip-surface depth is highly dependent on the quality of the InSAR monitoring data, while the accuracy of InSAR itself is influenced by multiple factors such as image coherence, sensor viewing geometry, temporal intervals, and surface-cover conditions. Consequently, certain areas may suffer from significant noise or discontinuous deformation retrievals, which can lead to discrepancies between the inverted slip-surface depth and actual conditions. This issue is particularly prominent for rapid-moving landslides, sudden failures, or slope bodies accompanied by large-scale collapses, where deformation occurs abruptly and varies sharply in space. In such cases, InSAR is unable to stably capture continuous deformation fields over short timescales, thereby reducing inversion reliability.

Moreover, the mass-conservation-based inversion approach assumes that the landslide mass remains essentially constant during movement. This assumption is more valid for creep-type and slow-moving deep-seated landslides, where deformation evolves gradually, continuously, and with relatively uniform internal material redistribution. It also holds reasonably well for landslides in loose soil, where sliding tends to be stable and coherent. However, for landslides involving significant block fall, material entrainment, undercutting, or large-scale detachment, the mass-conservation assumption breaks down. As a result, slip-surface inversion based on this method has limited accuracy for these types of failures.

Therefore, both InSAR data quality and the validity of the mass-conservation assumption jointly constrain the applicability of the slip-surface inversion method. For complex, rapidly deforming, or structurally unstable landslides, it is necessary to integrate additional datasets and complementary methods for a more reliable assessment.

5.2. Discussion on the Statistical Characteristics and Coupling Effects of Factors Influencing Slip-Surface Depth

GeoDetector analysis indicates that elevation is the primary influencing factor, and that interaction effects (e.g., "slope × elevation" and "aspect × elevation") exhibit significantly enhanced explanatory power. This suggests that slip-surface depth is not controlled by a single factor, but rather results from the coupling of multiple fields. This finding is consistent with conclusions from previous studies on creeping landslides and provides statistical evidence, from a spatial perspective, for the complex coupled mechanisms governing creeping landslide behavior. In addition, the typical landslide group selected in this study is geographically concentrated and shares a consistent geological background at the 1:25,000 scale (including lithology and geological structure). Accordingly, elevation, slope, aspect, and vegetation cover were selected as the influencing factors. However, high-resolution hydrological data, such as groundwater information at the individual landslide scale, were not available, and the influence of hydrological factors was therefore not explicitly considered. This limitation may result in an incomplete interpretation of deep-seated controlling mechanisms.

The landslide classification proposed in this study is based on the statistical characteristics of slip-surface geometry and is intended to characterize the statistical differences in slip-surface morphology and its relationship with topographic position among different landslides, thereby providing a structured diagnostic perspective for identifying their

potential deformation modes and evolutionary characteristics. On this basis, by establishing a conceptual correspondence between the statistical features of slip-surface geometry and classical landslide mechanical models, this study provides physical interpretations of deformation patterns for different landslide types, thereby enhancing the plausibility and interpretability of the statistical classification results within the framework of classical landslide mechanics.

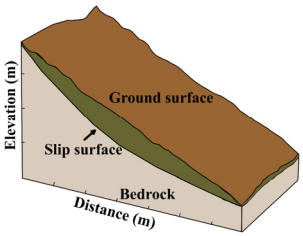
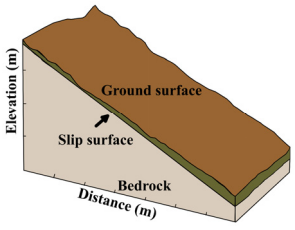
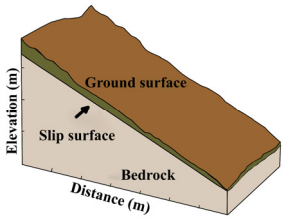
5.3. Coupling Mechanisms Between Sliding-Surface Structure and Landslide Mechanics

(1) Rotational Landslides

The sliding surface exhibits an arcuate pattern of "thin-thick-thin" from rear to front, reflecting the rotation of the landslide mass around a potential center of rotation. The rear edge is dominated by tensile stress, where tensile cracks develop and the sliding surface becomes shallow. The middle section forms the main shear zone, where shear stress concentrates and plastic deformation of the rock-soil mass leads to a thickened slip surface—this region serves as the mechanical fulcrum controlling moment equilibrium. The front edge is compression-controlled, and the slip surface either shears out along a weak plane or terminates at a shallow depth, forming a complete rotational failure mechanism [39,40].

The rotational landslides identified in this study (e.g., Taopingcun and Xiaoqicun No. 2) display a "middle-thick" statistical signature that perfectly corresponds to the main shear-band concept in circular sliding theory. The maximum depth zone coincides with the area of peak internal shear stress driven by gravity. Here, the sliding surface develops most deeply, forming a plastic deformation and material accumulation zone that provides resistance to large shear forces. The thin rear corresponds to the tension-crack zone, while the thin front corresponds to the compressive shear-out or resisting zone—together composing a complete rotational failure system (Table 8).

Table 8. Comparative table of landslide sliding-surface structural characteristics and mechanical mechanisms.

Landslide Type	Diagram of Landslide Types	Statistical Pattern	Corresponding Mechanical Model	Core Mechanical Process
Rotational Landslide		Medium depth (arcuate type)	Circular sliding model	Rotation occurs around the center of curvature; the main shear band reaches its maximum depth at the mid-slope to resist peak shear stress.
Push-type Translational Landslide		Thin top and thick bottom (descending type)	Active-passive model	The rear active zone provides thrust, while the front passive zone becomes compressed and accumulates, forming deep embedment and promoting downslope development of the sliding surface.
Traction-type Translational Landslide		Thick top and thin bottom (ascending type)	Progressive retrogression model	Failure initiates in shallow layers at the toe; loss of support triggers instability that propagates upslope, inducing deep shear development.

(2) Push-Type Translational Landslides

The sliding surface shows a "thin top-thick bottom" distribution. The rear portion acts as the driving zone, initiating along a shallow but steeply dipping weak plane and providing the downslope thrust [39–41]. The front portion acts as the resisting zone, where strong compression at the slope toe forces the formation of a deep sliding surface with a shovel-shaped geometry, representing the competition between driving and resisting forces consistent with the active-passive wedge model (Table 8).

For push-type translational landslides (e.g., Xishancun and Mashancun No. 1), the "thin top-thick bottom" pattern is well explained by the active-passive wedge mechanism. The rear segment behaves as the active block, initiating motion along a shallow weak plane and supplying the main driving force. The front segment behaves as the passive block, where movement becomes strongly impeded at the slope toe, generating intense compressive stress that forces the landslide to "dig" downward and accumulate material, resulting in significant deepening of the sliding surface. This pattern records the stress transfer from rear to front and the formation of deep shear due to strong frontal resistance.

(3) Traction-Type Translational Landslides

The sliding surface displays a "thick top-thin bottom" pattern. Failure initiates at the slope toe due to unloading or erosion, producing shallow shear. Instability subsequently propagates upslope, and the rear portion of the landslide mass, in order to overcome increasing resistance, connects to deeper weak planes or forms deeper shear zones [39,40]. This produces the characteristic configuration of a deep rear and shallow front, reflecting progressive retrogressive failure and stress redistribution (Table 8).

The traction-type landslides (e.g., Sanzhaicun) identified in this study exhibit a "thick top-thin bottom" depth pattern typical of progressive retrogressive failure. Initial shallow slip develops at the toe due to unloading or erosion. Instability then expands upslope; because the rear mass is larger and has higher potential energy, its movement encounters greater resistance and thus preferentially engages deeper weak layers or forms new deep shear bands. Consequently, the sliding surface becomes much deeper at the rear than at the front, representing the stress redistribution and self-optimization of the failure surface in response to boundary condition changes initiated at the toe.

This study identifies three typical types of creeping landslides based on the spatial statistical patterns of slip-surface depth. Their characteristics show good consistency with classical geomechanical models, reflecting the dominant failure mechanisms of different landslides. The three-dimensional distribution of slip-surface depth obtained from InSAR inversion not only represents the geometric characteristics of landslides, but also integrates information on their stress states, deformation mechanisms, and evolutionary stages. By combining statistical patterns with mechanical models, it is possible to achieve a transition from "form" to "state", that is, to infer the internal mechanical conditions and evolutionary stages of landslides from their observed morphological and structural features. It should be noted that natural landslides are commonly controlled by multiple coupled mechanisms, and the classification proposed in this study reflects their dominant deformation modes. In future work, the integration of more detailed geotechnical parameters and numerical simulations would allow further quantification of stress–strain relationships, thereby improving predictions of landslide stability and evolutionary trends.

6. Conclusions

This study focuses on typical creep-type landslides in Li County and establishes an integrated technical framework that combines SBAS-InSAR time-series deformation, mass-conservation-based slip-surface depth inversion, and GeoDetector factor diagnosis. This

framework enables the quantitative inversion of slip-surface depth, the identification of dominant controlling factors, and the analysis of their influencing mechanisms.

(1) InSAR deformation characteristics: The ascending and descending InSAR results from 2022 to 2024 show that deformation is mainly concentrated in the middle-upper portions of the slopes, with descending-track rates of −1 to −196 mm/year and ascending-track rates of −1 to −106 mm/year. Most of the eight landslides exhibit continuous downslope movement. The slope-parallel and slope-normal decomposition further reveals distinct deformation concentration zones for each landslide. SBAS-InSAR successfully captures the long-term and continuous deformation behavior of creep-type landslides.

(2) Slip-surface depth inversion: The mass-conservation-based inversion results agree well with borehole and profile data. The maximum sliding-surface depths range from 32 to 98 m and display strong spatial heterogeneity. Validation results show R^2 values greater than 0.92, correlation coefficients exceeding 0.97, and RMSE values of ±4.96 to ±16.56 m, indicating high overall accuracy of the inversion method.

(3) Controlling factors and mechanisms: The sliding-surface depth is primarily controlled by elevation and further influenced by the combined effects of slope, aspect, and other terrain factors. GeoDetector results show that all factors have $p < 0.05$ with significant q values; elevation independently explains 12.7–42.6% of the variance and is therefore the dominant controlling factor, while in some landslides, aspect accounts for as much as 30–45%. All interactions exhibit "bi-factor enhancement" or "nonlinear enhancement", indicating that sliding-surface depth is governed by the coupling of multiple factors rather than a single control. Boxplot statistics reveal three typical variation patterns of sliding-surface depth with elevation and slope: arc-shaped, decreasing, and increasing patterns. These correspond, respectively, to rotational landslides, push-type translational landslides, and traction-type translational landslides, each characterized by distinct geomorphological–mechanical relationships.

The three-dimensional sliding-surface geometry inverted from InSAR not only provides the spatial configuration of the failure surface but also represents a direct record of the slope's stress state, deformation mechanism, and evolutionary history. By integrating statistical patterns with mechanical models, the analysis enables a transition from "form" to "state", that is, inferring internal mechanical conditions and evolutionary stages based on the observed structural morphology.

Author Contributions: Y.S.: Writing—original draft, Methodology, Investigation, Formal analysis. X.W.: Writing—review and editing, Funding acquisition, Methodology. X.Y.: Writing—review and editing, Methodology. L.C.: Writing—original draft. H.G.: Writing—original draft. All authors have read and agreed to the published version of the manuscript.

Funding: This work is funded by the Key Science and Technology Plan of the Emergency Management Department (2024EMST030301), National Natural Science Foundation of China (U21A2013, 42571359, 42311530065), Innovative Research Groups of Hubei Province of China (Grant No. 2024AFA015), Opening Fund of Key Laboratory of Geological Survey and Evaluation of Ministry of Education (Grant Nos. GLAB2024ZR04, GLAB2020ZR02, GLAB2022ZR02), and the Fundamental Research Funds for the Central Universities, China University of Geosciences (Wuhan) (CUG2642022006).

Data Availability Statement: The original contributions presented in the study are included in the article, further inquiries can be directed to the corresponding author.

Acknowledgments: We acknowledge the Alaska Satellite Facility (ASF) for providing Sentinel-1A SAR imagery and DEM support for this study. We also thank the National Tibetan Plateau Data Center (TPDC) for supplying vegetation coverage data, and the Japan Aerospace Exploration Agency (JAXA) for providing the high-resolution DEM products.

Conflicts of Interest: The authors declare that they have no known competing financial interests or personal relationships that could have appeared to influence the work reported in this paper.

References

1. Van Asch, T.W.J. Creep processes in landslides. *Earth Surf. Process. Landf.* **1984**, *9*, 573–583.
2. Zhang, S.; Jiang, T.; Pei, X.; Huang, R.; Xu, Q.; Xie, Y.; Zhi, L. A new forecasting method for failure time of creep landslide based on nonlinear creep behavior and new pre-warning criterion. *Front. Earth Sci.* **2022**, *10*, 1018432. [CrossRef]
3. Puzrin, A.M.; Schmid, A. Progressive failure of a constrained creeping landslide. *Proc. R. Soc. A* **2011**, *467*, 2444–2461.
4. Shuzui, H. Process of slip-surface development and formation of slip-surface clay in landslides in Tertiary volcanic rocks, Japan. *Eng. Geol.* **2001**, *61*, 199–220.
5. Carter, M.; Bentley, S.P. The geometry of slip surfaces beneath landslides: Predictions from surface measurements. *Can. Geotech. J.* **1985**, *22*, 234–238. [CrossRef]
6. Kang, Y.; Lu, Z.; Zhao, C.; Qu, W. Inferring slip-surface geometry and volume of creeping landslides based on InSAR: A case study in Jinsha River Basin. *Remote Sens. Environ.* **2023**, *294*, 113620. [CrossRef]
7. Bishop, K.M. Determination of translational landslide slip surface depth using balanced cross sections. *Environ. Eng. Geosci.* **1999**, *2*, 147–156. [CrossRef]
8. Aryal, A.; Brooks, B.A.; Reid, M.E. Landslide subsurface slip geometry inferred from 3-D surface displacement fields. *Geophys. Res. Lett.* **2015**, *42*, 1411–1417. [CrossRef]
9. Bromhead, E.N. Landslide slip surfaces: Their origins, behaviour and geometry. *Landslides Eval. Stab.* **2004**, *1*, 3–21.
10. Zhang, Y.; Meng, X.; Jordan, C.; Novellino, A.; Dijkstra, T.; Chen, G. Investigating slow-moving landslides in the Zhouqu region of China using InSAR time series. *Landslides* **2018**, *15*, 1299–1315. [CrossRef]
11. Zhang, L.; Dai, K.; Deng, J.; Ge, D.; Liang, R.; Li, W.; Xu, Q. Identifying potential landslides by stacking-InSAR in southwestern China and its performance comparison with SBAS-InSAR. *Remote Sens.* **2021**, *13*, 3662. [CrossRef]
12. Kang, Y.; Zhao, C.; Zhang, Q.; Lu, Z.; Li, B. Application of InSAR techniques to an analysis of the Guanling landslide. *Remote Sens.* **2017**, *9*, 1046. [CrossRef]
13. Dai, K.; Li, Z.; Tomás, R.; Liu, G.; Yu, B.; Wang, X.; Stockamp, J. Monitoring activity at the Daguangbao mega-landslide (China) using Sentinel-1 TOPS time series interferometry. *Remote Sens. Environ.* **2016**, *186*, 501–513.
14. Yao, J.; Yao, X.; Liu, X. Landslide detection and mapping based on SBAS-InSAR and PS-InSAR: A case study in Gongjue County, Tibet, China. *Remote Sens.* **2022**, *14*, 4728. [CrossRef]
15. Dong, J.; Niu, R.; Li, B.; Xu, H.; Wang, S. Potential landslides identification based on temporal and spatial filtering of SBAS-InSAR results. *Geomat. Nat. Hazards Risk* **2023**, *14*, 52–75.
16. Booth, A.M.; McCarley, J.C.; Nelson, J. Multi-year, three-dimensional landslide surface deformation from repeat lidar and response to precipitation: Mill Gulch earthflow, California. *Landslides* **2020**, *17*, 1283–1296. [CrossRef]
17. Eriksen, H.Ø.; Lauknes, T.R.; Larsen, Y.; Corner, G.D.; Bergh, S.G.; Dehls, J.; Kierulf, H.P. Visualizing and interpreting surface displacement patterns on unstable slopes using multi-geometry satellite SAR interferometry (2D InSAR). *Remote Sens. Environ.* **2017**, *191*, 297–312. [CrossRef]
18. Booth, A.M.; Lamb, M.P.; Avouac, J.P.; Delacourt, C. Landslide velocity, depth, and rheology from remote sensing: La Clapière landslide, France. *Geophys. Res. Lett.* **2013**, *40*, 4299–4304. [CrossRef]
19. Jaboyedoff, M.; Carrea, D.; Derron, M.H.; Oppikofer, T.; Penna, I.M.; Rudaz, B. A review of methods used to estimate initial landslide failure surface depths and volumes. *Eng. Geol.* **2020**, *267*, 105478. [CrossRef]
20. Shen, Y.; Wang, X.; Dai, K.; Guo, H.; Yi, X.; Wang, X.; Zhuo, G. Inference of creep landslide slip surface by InSAR technology and improved particle swarm optimization. *Landslides* **2025**, *22*, 1665–1676. [CrossRef]
21. Hu, X.; Lu, Z.; Pierson, T.C.; Kramer, R.; George, D.L. Combining InSAR and GPS to determine transient movement and depth of a seasonally active low-gradient translational landslide. *Geophys. Res. Lett.* **2018**, *45*, 1453–1462. [CrossRef]
22. Handwerger, A.L.; Booth, A.M.; Huang, M.-H.; Fielding, E.J. Inferring the subsurface geometry and strength of slow-moving landslides using 3-D velocity measurements from UAVSAR. *J. Geophys. Res. Earth Surf.* **2021**, *126*, e2020JF005898. [CrossRef]
23. Zhu, W.; Yang, L.; Cheng, Y.; Liu, X.; Zhang, R. Active thickness estimation and failure simulation of translational landslide using multi-orbit InSAR observations: A case study of the Xiongba landslide. *Int. J. Appl. Earth Obs. Geoinf.* **2024**, *129*, 103801.
24. Guerriero, L.; Coe, J.A.; Revellino, P.; Grelle, G.; Pinto, F.; Guadagno, F.M. Influence of slip-surface geometry on earth-flow deformation, Montaguto earth flow, southern Italy. *Geomorphology* **2014**, *219*, 285–305. [CrossRef]
25. Wang, J.F.; Xu, C.D. Geographical detector: Principles and prospects. *Acta Geogr. Sin.* **2017**, *72*, 116–134.
26. Sun, D.; Shi, S.; Wen, H.; Xu, J.; Zhou, X.; Wu, J. A hybrid optimization method of factor screening predicated on GeoDetector and Random Forest for landslide susceptibility mapping. *Geomorphology* **2021**, *379*, 107623. [CrossRef]
27. Wang, Y.; Wen, H.; Sun, D.; Li, Y. Quantitative assessment of landslide risk based on susceptibility mapping using Random Forest and GeoDetector. *Remote Sens.* **2021**, *13*, 2625. [CrossRef]

28. Li, Y. Study on the Dynamic Strength Characteristics and Failure Mechanism of Glaciofluvial Deposits of the Xishancun Landslide in Li County. Master's Thesis, Chengdu University of Technology, Chengdu, China, 2020.
29. Yue, X. Stability Analysis of the Qingliucun Landslide in Li County. Master's Thesis, Southwest Jiaotong University, Chengdu, China, 2022.
30. Cheng, L. Stability Analysis and Hazard-Affected Area Prediction of the High-Elevation Lourocun Landslide in Li County. Master's Thesis, Chengdu University of Technology, Chengdu, China, 2021.
31. Zhu, L.; Meng, J.; Zhu, L. Applying Geodetector to disentangle the contributions of natural and anthropogenic factors to NDVI variations in the middle reaches of the Heihe River Basin. *Ecol. Indic.* **2020**, *117*, 106545. [CrossRef]
32. Wang, H.; Qin, F.; Xu, C.; Li, B.; Guo, L.; Wang, Z. Evaluating the suitability of urban development land with a Geodetector. *Ecol. Indic.* **2021**, *123*, 107339. [CrossRef]
33. Zhou, X.; Wen, H.; Zhang, Y.; Xu, J.; Zhang, W. Landslide susceptibility mapping using hybrid Random Forest with GeoDetector and RFE for factor optimization. *Geosci. Front.* **2021**, *12*, 101211. [CrossRef]
34. Chen, W.; Yang, L.; Wu, J.; Wu, J.; Wang, G.; Bian, J.; Zeng, J.; Liu, Z. Spatio-temporal characteristics and influencing factors of traditional villages in the Yangtze River Basin: A Geodetector model. *Herit. Sci.* **2023**, *11*, 111. [CrossRef]
35. Chen, J.; Ma, H.; Yang, S.; Zhou, Z.; Huang, J.; Chen, L. Assessment of urban resilience and detection of impact factors based on spatial autocorrelation analysis and Geodetector: A case of Hunan Province. *ISPRS Int. J. Geo-Inf.* **2023**, *12*, 391. [CrossRef]
36. Guo, Y.; Cheng, L.; Ding, A.; Yuan, Y.; Li, Z.; Hou, Y.; Zhang, S. Geodetector model-based quantitative analysis of vegetation change characteristics and driving forces: A case study in the Yongding River Basin, China. *Int. J. Appl. Earth Obs. Geoinf.* **2024**, *132*, 104027. [CrossRef]
37. Ma, X. Collaborative Early Warning Study of the Xishancun Landslide in Li County, Sichuan Province. Master's Thesis, Chengdu University of Technology, Chengdu, China, 2016.
38. Luo, J. Study on the Reactivation Mechanism and Key Disaster-Causing Factors of the Xishancun Landslide in Li County. Master's Thesis, Chengdu University of Technology, Chengdu, China, 2015.
39. Li, L.W. Displacement Prediction and Stability Evaluation Methods for Landslides in the Accumulation Layers Along the Three Gorges Reservoir Area. Ph.D. Thesis, China University of Geosciences, Wuhan, China, 2021.
40. Wang, G.; Xu, R.; Liu, G. *Landslide Science and Landslide Prevention Technology*; China Railway Publishing House: Beijing, China, 2004.
41. Angeli, M.G.; Pasuto, A.; Silvano, S. A critical review of landslide monitoring experiences. *Eng. Geol.* **2000**, *55*, 133–147. [CrossRef]

Disclaimer/Publisher's Note: The statements, opinions and data contained in all publications are solely those of the individual author(s) and contributor(s) and not of MDPI and/or the editor(s). MDPI and/or the editor(s) disclaim responsibility for any injury to people or property resulting from any ideas, methods, instructions or products referred to in the content.